Synoptic conditions and frontal dynamics during Cold Air Outbreaks in the Norwegian and Barents Sea

Master's thesis in meteorology

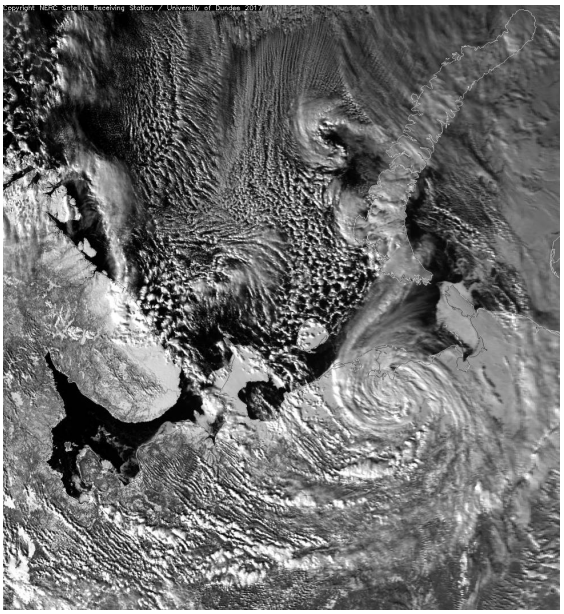

Marit Dagny Kristine Jenssen

August 6, 2018

UNIVERSITY OF BERGEN
GEOPHYSICAL INSTITUTE

The picture on the front page is a satellite picture of a polar low over north-west Russia at March 31, 2017. In the Barents Sea, west of Novaya Zemlya there is also a cold air outbreak. The picture is downloaded from NERC Satellite Receiving Station, Dundee University, Scotland (http://www.sat.dundee.ac.uk/).

Abstract

Cold Air Outbreaks (CAOs) in the Norwegian and Barents Sea are investigated using ERA Interim. The focus is on the synoptic conditions, heat fluxes, potential temperature tendencies and the frontogenesis at the onset of the CAOs. Four regions are investigated using the time series of the mean CAO index inside each region. Composite analysis is the core of this work.

CAOs in each region are detected and separated with respect to the mean wind direction at 900 hPa at the time step where the CAOs are on their most intense stage. Composites for the different types of CAOs in the different regions are calculated. The separation shows that most CAOs are associated with northerlies when the mean CAO index is maximum. The composite analysis is supplemented by two case studies, one of a CAO in the Fram Strait, December 22–27, 2015 and another one in the Barents Sea, January 11–20, 2015. The results from the case and composite studies are compared, and they resemble each other.

One of the main conclusions from this work is that there is typically a large scale cyclone advecting cold air off the ice edge. In addition, there is often some baroclinic growth at the onset of and during CAOs. It is confirmed that CAOs are associated with sensible and latent heat fluxes, and hence diabatic heating, which is already well established from the literature.

The different contributions to frontogenesis along the CAO front are investigated through both the case and the composite studies, using the frontogenesis function. It is found that CAOs in the Fram Strait associated with northerlies are associated with stronger circulation than CAOs in the Barents Sea associated with easterlies.

Acknowledgements

First of all, I would like to thank my supervisors Thomas Spengler and Lukas Papritz for offering me an exciting topic for a master's thesis. During the last year I have gone from needing a lot of guidance to be more independently thinking. Thomas and Lukas have contributed a lot to that. Thank you for fruitful discussions by e-mail and in person and for constructive feedback on my writing. And thank you for convincing me that I didn't need any postponement on the deadline and for never giving up on me. Special thanks to Thomas for countless revisions and comments during the last month.

Clemens Spensberger deserves a huge thanks for answering all my questions regarding Python and Dynlib, by e-mail and in person. Also, thanks for input on the physical interpretation on my results when Thomas and Lukas were not at GFI. Thanks to the rest of the dynamical meteorology group at GFI for nice Monday meetings during the last year. It has been good to have some forced breaks from my work.

Erik Kolstad, Asgeir Sorteberg, Sigrunn H. Sørbye and Tor Eldevik have all given me input on the significance test. Many thanks for that. And again, thanks to Lukas for a fruitful discussion on the topic. I learned a lot from that. Finally I managed to perform the test. Thanks to Erik for help with calculating anomalies although I ended up with not showing any anomalies in my thesis.

Thanks to my classmate from high school Johannes Larsen for showing me how to use dictionaries in Python and for proofreading.

Thanks to my fellow students for three nice years at GFI. Special thanks to Kjersti Konstali for telling me to go home in the afternoons and not put too much pressure on myself.

A special thanks goes to the cafeteria employees at GFI. Your tasty, healthy and cheap lunch has helped a lot on my motivation and wellbeing during my last semester at GFI.

In the end I want to thank my boyfriend Magnar Bjørgve for providing me with an online Python course at the beginning of my thesis. Furthermore, thanks for all help with LaTeX, for supporting me during the entire time I have spent on my thesis, for convincing me that everything will be fine and for always believing in me.

Contents

List of Figures

List of Tables

Acronyms

4D–VAR 4-Dimensional VARiational data assimilation.

ACF AutoCorrelation Function.

ASR Arctic System Reanalysis.

CAO Cold Air Outbreak.

CMIP Coupled Model Intercomparison Project.

ECMWF European Center for Medium Range Weather Forecasting.

ERA ECMWF ReAnalysis.

FWER Family Wise Error Rate.

GFI Geophysical Institute.

hPa hectopascal.

MSLP Mean Sea Level Pressure.

NaN Not a Number.

SST Sea Surface Temperature.

Z500 geopotential height at 500 hPa.

Z900 geopotential height at 900 hPa.

Chapter 1

Introduction

Cold Air Outbreaks (CAOs) are weather events where cold air residing over ice is advected over relatively warmer ocean. They occur on both hemispheres at higher latitudes during all seasons (Fletcher et al., 2016), though they appear more frequently during the winter seasons. Understanding CAOs and how they occur is important because they play a significant role for weather and climate at higher latitudes. For instance, CAOs contribute to the major part of wintertime cooling of the ocean (Papritz and Spengler, 2017). Hence, CAOs are essential for deep water formation and the Atlantic meridional overturning circulation. CAOs can also lead to severe weather such as polar lows (Businger, 1985; Carleton and Song, 1997).

Polar lows are mesoscale (horizontal scale of 20–2000 km, Markowski and Richardson (2011)) cyclones. They occur when cold air has moved off the ice edge (a CAO) and is sitting over the relatively warmer ocean. Then heat fluxes occur (Renfrew and Moore, 1999) and the air mass receives heat and moisture from the ocean. This leads to extreme weather, such as strong winds and snow showers (Rasmussen and Turner, 2003). This kind of weather is potentially dangerous to oceanic activities such as fishing, shipping and oil extraction. Polar lows can also hit land and cause damage to coastal settlements. However, these events are very short lived since polar lows are dependent on supplies of heat from the ocean.

This thesis focuses on CAOs in the Norwegian and Barents Sea during the expanded Northern Hemisphere winter season from November 1st to 30th of April. Four latitude-longitude boxes are strategically chosen: East Greenland, the Fram Strait, the Barents Sea and the Norwegian coast, represented by boxes (a)–(d), respectively in Figure 1.1. CAOs in each of these boxes are detected using a time series analysis explained in section 2.5. When the CAOs are detected, their prop-

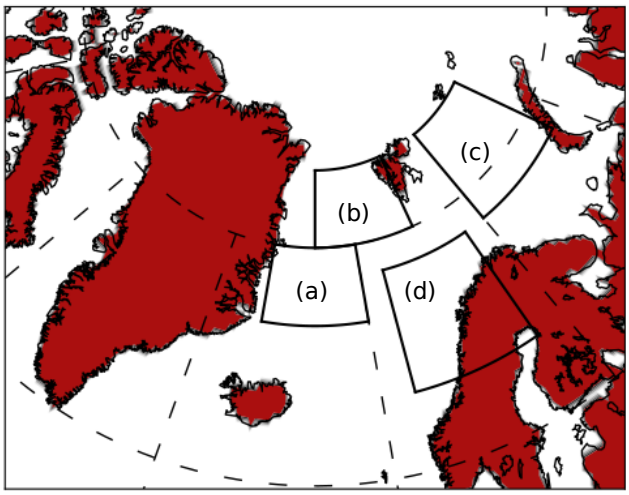

Figure 1.1: Map of the Norwegian and Barents Sea. The regions investigated in this thesis are shown with latitude-longitude boxes. Four regions are chosen: East Greenland (a), the Fram Strait (b), the Barents Sea (c) and the Norwegian coast (d).

erties are investigated through case and composite studies, where the purpose is to answer some questions on the synoptic conditions and the frontal dynamics. To summarize, the following questions are addressed:

1. Is there a typical synoptic situation associated with CAOs?
2. How are the frontal dynamics during CAOs?
3. Do CAOs have different properties in the different regions?

These questions are investigated through composite analysis (chapter 4), where all events inside each box are studied together. Composites are useful to get an overall view of what is going on during CAOs. Two case studies (chapter 3) are performed in order to supplement the composite analysis. The first case study is of a CAO that occurred in the Fram Strait in the period December 23–27, 2015. The second case study investigates a CAO that occurred in the Barents Sea region in the period January 11–20, 2015 is performed. Analysis of the composites shows that the details of each event tend to be smeared out, so it is useful to additionally look at a few isolated events. Even though the details are smeared out, the overall structure of the composites resembles the case studies. The composites also work as a supplement to the case studies because when only one or two CAOs are

studied, it is difficult to say anything about CAOs in general. In other words, case and composite studies complement each other.

Chapter 2

Data, theory and methods

This chapter presents the data and the methods used in this work. The dataset is produced by European Center for Medium Range Weather Forecasting (ECMWF) and it is called ECMWF ReAnalysis (ERA) Interim. First, ERA Interim is presented, followed by an explanation of how the dataset is produced, and the potential temperature and the CAO index is defined. Next, the procedure for choosing regions is explained and the time series analysis used to determine a threshold of the CAO index is presented. When CAOs are detected, the events are separated with respect to the wind direction at 900 hectopascal (hPa) at the time step when the CAO is on the most intense stage. The procedure of the separation is explained in section 2.6. Then the composite analysis is explained, followed by the approach for the field significance test on the composites. Next, the frontogenesis function is introduced together with the Sawyer–Eliassen equation. In the end of this chapter the procedure of vertically averaging the potential temperature tendency is explained.

2.1 Data

The ECMWF produced the ERA Interim dataset used in this thesis (Dee et al., 2011). The data are available on a $0.75^\circ \times 0.75^\circ$ longitude-latitude grid for the time period 1979–2016 with a time increment of 6 hours, and on 60 vertical levels in pressure coordinates. At the Geophysical Institute (GFI) the data are interpolated to a $0.5^\circ \times 0.5^\circ$ longitude-latitude grid due to consistency with other datasets.

Reanalysis data are produced by data assimilation. In a data assimilation procedure observations and forecasts are combined in order to provide an estimate of the

atmospheric state that is as close to reality as possible. There are several types of data assimilation. ERA Interim is generated by the method called 4-Dimensional VARiational data assimilation (4D–VAR). The purpose of this method is to find the analysis (combination of observation and forecast) that minimizes a cost function (Warner, 2010). The cost function is a measure of the distance of the analysis to both the observation and the forecast. One advantage with using reanalysis instead of forecast in research is that the observations and forecasts are assimilated together. If the forecast is not good enough, it will be corrected by the observation[1].

Heat fluxes, radiation, diabatic heating, precipitation and evaporation are not part of the reanalysis. These variables are parameterized from the model. The values are 6 hourly accumulated from 3 hours before a certain time step to 3 ours after the time step. For example, the sensible heat flux at 06:00 is accumulated from 03:00 to 09:00. Next, it is divided by 6 hours so that the unit for heat flux in ERA Interim is $\mathrm{Jm}^{-2}(6\mathrm{h})^{-1}$.

2.2 Potential temperature

Following Wallace and Hobbs (2006), the potential temperature is the temperature a dry air parcel would have if it was brought adiabatically from its existing pressure to a standard pressure, generally taken as 1000 hPa. The equation for the potential temperature at some pressure level p is

$$\theta = T\left(\frac{p_0}{p}\right)^{R/c_p}, \tag{2.1}$$

where T is the actual temperature and p_0 is a reference pressure (typically 1000 hPa). R is the gas constant of dry air (287 $\mathrm{JK}^{-1}\mathrm{kg}^{-1}$), and c_p is the specific heat of dry air at constant pressure (1004 $\mathrm{JK}^{-1}\mathrm{kg}^{-1}$). Potential temperature is conserved in adiabatic processes, where an adiabatic process is a process where there is no heat exchange with the surroundings. There are no purely adiabatic flows in the atmosphere, but there are flows that approximate adiabatic.

Although CAOs are diabatic flows, potential temperatures are useful because they allow for comparing air parcels at different pressure levels. Assuming an air parcel at 1015 hPa (a typical value for the Mean Sea Level Pressure (MSLP)) with temperature equal to the Sea Surface Temperature (SST) and another air parcel at

[1]Data assimilation is also used in weather forecasting in order to find initial conditions that are as good as possible.

900 hPa with temperature equal to T_{900}, the question is: Which temperatures will these air parcels have if they are brought adiabatically to the reference pressure of 1000 hPa.

In the next section (section 2.3), the CAO index is defined as a potential temperature difference between the sea surface and 900 hPa. This difference tells how much energy can potentially be added to the atmosphere until there would be no more heat fluxes from the ocean. When there are no more heat fluxes, the potential temperature of the air is the same as that of the sea surface.

2.3 CAO index

A CAO index often consists of the potential temperature at the surface minus the potential temperature at a certain pressure level (Papritz et al., 2015; Papritz and Spengler, 2017; Kolstad et al., 2009; Bracegirdle and Kolstad, 2010; Fletcher et al., 2016). Then a positive CAO index means that the surface is warmer than the air at a certain pressure level. During a CAO the air is colder than the surface, which means that the CAO index combined with a threshold ($\Delta\theta_{thresh}$, section 2.5) can tell whether there is a CAO or not.

The choice of CAO index depends on the properties of interest. For instance, Kolstad and Bracegirdle (2008) and Kolstad et al. (2009) used a CAO index defined as

$$\mu = \frac{\Delta\theta}{\Delta p} = \frac{\theta_{SKT} - \theta_{700}}{p_{sl} - p_{700}}, \tag{2.2}$$

where θ_{SKT} is the potential skin temperature, p_{700} is 700 hPa, θ_{700} is the potential temperature at 700 hPa and p_{sl} is the sea level pressure. This CAO index focuses on stability and is useful for investigating conditions for polar lows. High μ values indicate that the denominator in equation (2.2) is low and hence the sea level pressure is low. This indicates low stability, hence good conditions for polar lows. Fletcher et al. (2016) used the CAO index $M = \theta_{SKT} - \theta_{800}$, where they found that using the 800 hPa level produced more high-latitude CAOs than the 700 hPa level. Bracegirdle and Kolstad (2010) and Kolstad (2011) used a dimensionless CAO index that should be more straightforward to interpret than the CAO index used in their previous studies (Kolstad and Bracegirdle, 2008; Kolstad et al., 2009), as it is aligned to actual sea-air differences in potential temperature.

Here the CAO index is defined as

$$\Delta\theta = \theta_{SST} - \theta_{900}, \tag{2.3}$$

Correlation between different CAO indices

	$\theta_{SST} - \theta_{850}$	$\theta_{SST} - \theta_{800}$	$\frac{L}{z_{700}} \ln \frac{\theta_{SST}}{\theta_{700}}$	$\frac{\theta_{SST} - \theta_{700}}{p_{sl} - p_{700}}$	$\theta_{SST} - \theta_{900}$
$\theta_{SST} - \theta_{850}$	1	0.983	0.908	0.910	0.978
$\theta_{SST} - \theta_{800}$	-	1	0.957	0.959	0.936
$\frac{L}{z_{700}} \ln \frac{\theta_{SST}}{\theta_{700}}$	-	-	1	0.999	0.847
$\frac{\theta_{SST} - \theta_{700}}{p_{sl} - p_{700}}$	-	-	-	1	0.850
$\theta_{SST} - \theta_{900}$	-	-	-	-	1

Table 2.1: Correlation between the CAO indices used in Papritz et al. (2015), Fletcher et al. (2016), Bracegirdle and Kolstad (2010), Kolstad et al. (2009) and this thesis, respectively. The correlations are calculated using the time series of the mean CAO index in the Fram Strait. The L in the CAO index by Bracegirdle and Kolstad (2010) is a scaling height of $7.5 \cdot 10^5$ m and z_{700} is the geopotential height at 700 hPa.

where θ_{SST} is the potential temperature at the sea surface and θ_{900} is the potential temperature at 900 hPa. The pressure level 900 hPa is used because CAOs can be shallow near the ice edge and may not have a signal at a pressure level less than 900 hPa. In grid points where the fraction of sea ice is close to 1, the SST may be set to freezing temperature, which would result in erroneous values of the CAO index. To handle this the CAO index values in grid points with sea ice cover larger than 0.5 are set to Not a Number (NaN).

The different CAO indices should be highly correlated since they describe the same events. In Table 2.1 the time series (for details see section 2.4 and section 2.5) of the mean CAO indices in the Fram Strait are calculated. Then the Pearson correlation coefficient between these different time series is calculated. The Pearson correlation coefficient between two samples $\mathbf{x} = x_1, ..., x_n$ and $\mathbf{y} = y_1, ..., y_n$ is defined as (Walpole et al., 2014)

$$r = \frac{\sum_{i=1}^{n}(x_i - \overline{x})(y_i - \overline{y})}{\sqrt{\sum_{i=1}^{n}(x_i - \overline{x})^2}\sqrt{\sum_{i=1}^{n}(y_i - \overline{y})^2}}, \tag{2.4}$$

where $\overline{x}$ and $\overline{y}$ are the sample means. The correlation describes the linear relation between two samples. If the correlation is equal to 0, then the two samples are completely linearly independent. A correlation equal to 1 or -1 means that the samples are linear combinations of each other. Table 2.1 shows that all CAO indices are highly positively correlated, as all correlation values are greater than 0.84. This means that if one CAO index is increasing, the others also do. If the different CAO indices are plotted against each other in a scatter plot, the points would lie on a straight diagonal line, increasing to the right (not shown).

2.4 Choosing regions

The regions investigated in this thesis are shown in Figure 1.1. When choosing regions it is important to make sure that no region is fully covered by sea ice. If this is the case, events in a certain region are missed, since the CAO index will not be defined. When the mean CAO index inside each region at each time step is calculated, grid points where the CAO index is not defined are ignored.

It is possible to decide which regions to investigate in different ways. For instance Kolstad et al. (2009) calculated the 90th percentiles of the CAO index during December–February in the period investigated, and the regions with the largest 90th percentiles where used in further analysis. However, it is well known that CAOs occur at higher latitudes. Hence, it is also reasonable to just choose some regions over the sea as done in this work.

2.5 Time series analysis

The time series of the mean CAO index, $\Delta\theta$ over a certain domain are calculated, where the purpose is to determine $\Delta\theta_{thresh}$. A CAO starts when the time series of the mean CAO index exceeds a certain threshold $\Delta\theta_{thresh}$, and ends when it drops below the threshold again. The first step of the procedure for detecting CAOs is to find the mean CAO index inside each of the boxes to investigate (Figure 1.1).

Let N_j be the number of grid points with sea ice cover of less than or equal to 0.5 at time step j inside one of the latitude-longitude boxes presented in chapter 1. If $\Delta\theta_{ij}$ is the CAO index in grid point i at time step j, then the mean CAO index at this time step is defined as

$$\overline{\Delta\theta}_j = \frac{1}{N_j} \sum_{i=1}^{N_j} \Delta\theta_{ij}. \tag{2.5}$$

Now the time series of the mean CAO index inside each region are calculated. Then it is used to find a threshold $\Delta\theta_{thresh}$, which is used to define when a CAO starts and ends.

One way to determine $\Delta\theta_{thresh}$ is to calculate a percentile of all the positive values in the time series of the mean CAO index. To find a percentile of a dataset, all the values are sorted in ascending order. The mth percentile is the value at

which m percent of the values fall below. For example, 25 % of the values in a dataset are below the 25th percentile. The 50th percentile represents the median of the dataset. Using all positive values has the disadvantage that long lived events contribute much more to the percentile than short lived ones. Instead, only selected local maxima in the time series are included. The selection of local maxima to use in the threshold calculation is explained below.

Figure 2.1a shows a time series of the spatial mean CAO index (for details see section 2.4) in the Fram Strait for the winter 2015/2016. The original time series has many short term fluctuations, which means that it is very noisy and contains several local maxima. It is not optimal to use all these local maxima to determine $\Delta\theta_{thresh}$, because only the local maxima that are actually peaks in the time series are interesting. Instead, the running mean is used. For this work the daily variation of the time series is interesting because CAOs typically last over days. Smith and Sheridan (2018) did a study of CAOs in the eastern United States where they found that the average duration of the CAOs investigated was approximately 6–8 days. The running mean is useful when long term variations are more interesting than short term fluctuations, because it smooths out the time series and removes some of the short term fluctuations, dependent on the window used. This makes it easier to study long term variations.

To calculate a running mean, one has to determine a suitable window (how many values to calculate mean of). If the window is equal to $2n + 1$, the running mean $x_{RM}(t)$ of a time series $x(t)$ is defined as

$$x_{RM}(t) = \frac{1}{2n+1} \sum_{i=-n}^{n} x(t+i), \tag{2.6}$$

with n equal to a positive integer. As an example, if n is equal to 2 (window equal to 5), the running mean is

$$x_{RM}(t) = \frac{1}{5} \left(x(t-2) + x(t-1) + x(t) + x(t+1) + x(t+2) \right). \tag{2.7}$$

The window should be an odd number so that the smoothed time series is not shifted and the peaks in the original time series and the running mean are at the same index. This is ensured in Equation 2.6 as $2n + 1$ will always be a positive odd number if n is a positive integer. To find a suitable window for the running mean, the AutoCorrelation Function (ACF) of the original time series is useful.

The ACF of a random variable is the correlation of a variable with itself. Temporal autocorrelation is the correlation of a variable with its own future and past values (Wilks, 2011; Shumway and Stoffer, 2017). The ACF gives an indication of the

memory in the time series. Following Shumway and Stoffer (2017), it is assumed that the time series are weakly stationary, which means that the autocovariance function only depends on the time lag h. The sample *autocovariance function* is defined as

$$\hat{\gamma}(h) = \frac{1}{n}\sum_{t=1}^{n-h}(x_{t+h} - \overline{x})(x_t - \overline{x}), \tag{2.8}$$

where $\overline{x}$ is the sample mean,

$$\overline{x} = \frac{1}{n}\sum_{t=1}^{n} x_t. \tag{2.9}$$

This gives the sample ACF

$$\hat{\rho}(h) = \frac{\hat{\gamma}(h)}{\hat{\gamma}(0)}. \tag{2.10}$$

At time lag 0 the ACF is equal to 1, $\hat{\gamma}(h = 0) = 1$, and it is less than 1 at larger time lags. If the ACF drops below 0.5 at time step n, then $2n + 1$ is a suitable window for the running mean.

Time series of the mean CAO index in all boxes (for details see section 2.4) for all winters (1979/1980–2015/2016) are calculated. This means that there are 37 time series for each box. In total there are $37 \cdot 4 = 148$ time series, since there are four boxes. The ACFs of all 148 time series are calculated. Then, for each ACF, the first time step where the ACF is less than 0.5 is found. This gives a list of 148 values. In the end the mean of these values is calculated. The mean time step at which the ACF drops below 0.5 is approximately 9.4. The window in this work is chosen to 17, which means that n in Equation 2.6 is equal to 8. It is convenient to set n equal to 8 because the dataset contains values at 4 points a day. When the running mean is calculated with this window, the first and last two days in the original time series are lost. This problem is solved by including 30th and 31st of October in the beginning and 1st and 2nd of May in the end so that the running mean starts at 1st of November and ends at 30th of April.

Figure 2.1b shows the time series in Figure 2.1a together with the running mean with window equal to 17. Now most of the short term fluctuations are removed, but the running mean still contains some local maxima that are not peaks and that should not be included when calculating the threshold. This is solved by defining a minimum distance between two local maxima. If the distance between two local maxima in the running mean is less than 10 time steps, only the largest of these is used.

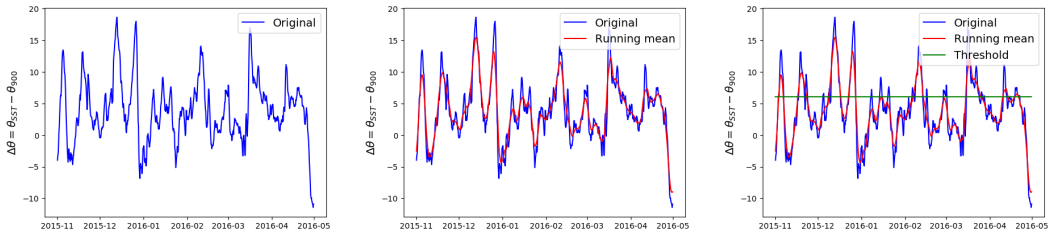

Figure 2.1: Timeseries of mean CAO index in Fram Strait during the winter 2015/2016 with running mean and threshold. An event starts when the running mean exceeds the threshold and ends when it drops below the threshold again.

The local maxima that will be included in the threshold calculation are calculated for all four regions and put in a list. Then the 50th percentile of these maxima is calculated and used as a threshold for the CAO index. The events are defined by the running mean of the time series and the threshold. Figure 2.1c shows the original time series, the running mean and the threshold together. Events that have duration shorter than one day are discarded, since these very short lived events (if they are events at all) can disturb the composites (for details see section 2.7) as they are not associated with a clear synoptic pattern. The winter shown in Figure 2.1c contains seven events. At the end of the winter, the running mean is slightly above the threshold, but this is not detected as an event because the duration is too short.

To summarize, the approach for determining $\Delta\theta_{thresh}$ is as follows:

1. Calculate time series for the mean CAO index within each box.

2. Calculate the running mean time series with window equal to 17.

3. Make a list of the local maxima in the running mean time series. Find the distance between the local maxima. If the distance between two maxima is less than 10 time steps, only include the largest of the two maxima in the list.

4. Perform step 1, 2 and 3 for all boxes and put all maxima together in a list.

5. Calculate the 50th percentile of all maxima in the list and use this number as $\Delta\theta_{thresh}$.

Performing this approach gives a $\Delta\theta_{thresh}$ equal to approximately 6.1 K. This is used with the running mean to define CAOs.

2.6 Separation of CAOs with respect to wind directions

As mentioned in chapter 1, four boxes in the Norwegian Sea and Barents Sea are chosen. Within each box there could be CAOs from different directions. For example, in the Barents Sea cold air could come both from the north and from the east. In Fram Strait there could be CAOs from Greenland (the west). It is therefore reasonable to separate events associated with different wind directions in order to not detect the same events in different boxes. In addition, the events are associated with different synoptic situations.

The time series of the mean wind at 900 hPa within each box at dates where the CAO index is maximum within each event are calculated. The mean wind direction at these dates is used as a criterion for putting the events into the different categories; north, south, east or west.

Let u be the zonal component of the mean wind inside a certain region and let v be the meridional component. For events where the mean wind is predominantly from the north, the mean wind inside the box is required to come from the north $\pm$ 45°, i. e.

$$v < 0 \quad \text{and} \quad |u| < |v|. \tag{2.11}$$

Similarly, if the mean wind is required to come predominantly from the east, the criterion is

$$u < 0 \quad \text{and} \quad |u| > |v|. \tag{2.12}$$

The criterion for predominantly westerly mean wind is

$$u > 0 \quad \text{and} \quad |u| > |v|, \tag{2.13}$$

and for predominantly southerly mean wind

$$v > 0 \quad \text{and} \quad |u| < |v|. \tag{2.14}$$

One may think it is reasonable to use the wind direction at the onset dates to separate the events, to detect where the cold air is actually coming from. The problem is that at the onset the box is probably not so affected by the CAO air mass, i.e., the front at the ice edge is still well defined. This means that the mean wind inside the box would not be representative for the transport of the CAO air mass.

2.7 Composite analysis

In a composite analysis, several events of the same type are investigated simultaneously. A large number of events is collected and the mean value over these events is calculated:

$$\text{com} = \frac{1}{N_C} \sum_n C_n S_n. \tag{2.15}$$

N_C is the number of contributions to the composite and S_n is a variable, for example MSLP. C_n is a dummy variable which is equal to 1 if the value at that time step should be included in the composite and 0 otherwise. If the composite is based on the largest peaks, the composite gives an impression on how the typical synoptic situation is when a CAO is on its most intense stage. A composite based on the onset of each CAO give an indication of what is typically going on at the onset of a CAO. The composite standard deviation gives an indication about the spread in the meteorological variables at the time steps included in the composite. It is defined as

$$s = \sqrt{\frac{1}{N_C - 1} \sum_n (S_n - \text{com})^2}. \tag{2.16}$$

If the composite standard deviation is high, the composite is not very representative for all events. Composites tend to smear out the details in each event because the members in the composites may be very different, and then the mean value may not be representative for all the composite members. Therefore it is useful to do case studies to supplement the composite analysis.

2.8 Significance test

Significance testing is used to check whether the composites are significant. If a composite is significant, it is unlikely that one gets the same composite by choosing random time steps. For instance, if the composite of MSLP during CAOs in the Fram Strait turns out to be significant, it means that it is likely the MSLP is special for CAOs.

The first step in a composite significance test is to generate the random time steps. When generating random dates, the dates that the original composite is based on are maintained, but the year is replaced by a random year from 1979 to 2016 (the years available in ERA Interim). For example, if the first date is

November 20, 1979, the first date in the random list is November 20 at a random year. This procedure for generating artificial composites for significance testing is also used in Kolstad et al. (2009). A large number of artificial composites is needed because it is necessary to assume that they have a symmetric distribution in order to perform the local hypothesis tests (explained below). In this work the number is chosen to 10 000, although 1000 might have been sufficient. When more than 1000 artificial composites are calculated, the result is almost the same (for details see section 4.5). 10 000 list of dates with random years are generated, and 10 000 artificial composites are calculated. The 10 000 artificial composites have a certain distribution, and the purpose of the significance test is to test whether the actual composite comes from the distribution of the 10 000 artificial composites.

Since one hypothesis test for each grid point is performed, it is not good enough to just reject the null hypothesis H_0 in grid points where the p-value (the probability of getting a result at least as extreme as the observation, given that the null hypothesis is true) is less than some significance level α (say 5 %) and maintain it elsewhere. The reason is that several hypothesis tests are performed simultaneously, which increases the probability of rejecting null hypotheses that are in fact true. It is necessary to perform a *field significance test* (Ventura et al., 2004) when several hypotheses are tested.

For instance, if 10 000 hypothesis tests are performed, all the null hypotheses are true and the chosen significance level is 5 %, 500 correct null hypotheses will on average be falsely rejected, which is not optimal. A field test is used to control the number of erroneously rejected null hypotheses. This can be controlled by the Family Wise Error Rate (FWER) (Benjamini and Hochberg, 1995), which is an upper limit for the proportion of falsely rejected null hypotheses among all rejected null hypotheses.

The second step of the field significance test is to define local and global null and alternative hypotheses. Assuming n local tests are performed, where n is the number of grid points, local hypotheses can be formulated:

$$H_i^0 : \text{The composite in grid point } i \text{ is random}$$
$$H_i^a : \text{The composite in grid point } i \text{ is not random,}$$

where $i = 1, ..., n$. The global hypotheses are

H_{global}^0 : The composite value in each grid point is random.
All local null hypotheses are true.

H_{global}^a : The composite value is not random for at least one grid point.
At least one local null hypothesis is false.

The next step is performing the local tests. Since the random composites are most likely not normally (Gaussian) distributed, it is necessary to perform a non-parametric test for the local hypotheses. A non-parametric, or distribution free test does not assume that the data have a certain distribution, e.g., normal distribution.

One alternative for a non-parametric test is the Wilcoxon signed-rank test (Walpole et al., 2014). This test is used to test if the median μ of a dataset is equal to a certain value. The assumption is that the dataset has a continuous and symmetric distribution. All meteorological variables used in this work are continuous, which makes it reasonable to assume a continuous distribution.

As mentioned, n is the number of grid points and hence the number of local hypothesis tests performed. If the composite in grid point i comes from the distribution of random composites, then the median of the random composites $\tilde{\mu}_i$ should be close to the composite in that grid point $\tilde{\mu}_{0,i}$. The local hypotheses can then be defined as

$$H_i^0 : \tilde{\mu}_i = \tilde{\mu}_{0,i}$$
$$H_i^a : \tilde{\mu}_i \neq \tilde{\mu}_{0,i},$$

which gives a two-sided test. For each grid point i, assume independent random composites $X_{i1}, ..., X_{im}$, with m equal to 10 000 in this case and define

$$Y_{ij} = X_{ij} - \tilde{\mu}_{0,i}, \quad i = 1, .., n, \quad j = 1, ..., m,$$

and sort Y_{ij} by the absolute value, $|Y_{ij}|$, in ascending order. All values are given ranks, and rank sums are calculated. w_+ is the sum of the ranks of all positive Y_{ij}, and w_- is the sum of the ranks of all negative Y_{ij}. Values of Y_{ij} equal to 0 are discarded. For a two-sided test, the test statistic is $w = \min(w_-, w_+)$. Performing the local tests will give a list of n p-values $p_1, ..., p_n$ for each individual test in each grid point. Benjamini and Hochberg (1995) developed a procedure for the local tests, where it is assumed that the local tests are independent. If $p_1 \leq p_2 \leq \cdots \leq p_n$ are the ordered p-values, the multiple-testing procedure is defined as

$$k = \max_{i=1,...,n} \left\{ i : p_i \leq \frac{i}{n} q \right\}. \tag{2.17}$$

This is a Bonferroni-type testing procedure. All $H_1^0, ..., H_k^0$ are rejected. q is the selected FWER. If no such k exists as defined in Equation 2.17, no local null hypotheses can be rejected. Benjamini and Yekutieli (2001) developed a procedure that does not assume independent local tests. According to Ventura et al. (2004) this procedure is too conservative (too difficult to reject any null hypotheses),

and Benjamini and Hochberg (1995) can be applied although the local tests are dependent. Furthermore, if the assumption of independence were not made, it would be very tedious to find the p-value of the global test. Then the binomial distribution could not have been used as it assumes independent trials.

H_0^{global} can be rejected if the p-value of the global test is less than some significance level α_{global} (Wilks, 2006). Let M be the discrete random variable describing the number of falsely rejected local null hypotheses. Then the p-value of the global test is the probability that M is greater than the observed value m given that H_0^{global} is correct. The requirement for rejecting H_0^{global} is

$$P\left(M \geq m | \, H_0^{global}\right) \leq \alpha_{global}. \tag{2.18}$$

Assumed that the local tests are independent, M can be described as a binomially distributed random variable under the null hypothesis. The number of trials is the number of local hypotheses, n, and p is the probability of rejecting a true null hypothesis. Then the probability that M is greater than m given H_0^{global} can be expressed as

$$P\left(M \geq m | H_0^{global}\right) = 1 - P\left(M \leq m-1 | H_0^{global}\right) = 1 - \sum_{x=0}^{m-1} \binom{n}{x} p^x (1-p)^{n-x}, \tag{2.19}$$

and H_0^{global} is rejected if $P(M \geq |H_0^{global} m)$ is less than the significance level α_{global}.

2.9 Frontogenesis

Frontogenesis is the process of increasing the magnitude of the potential temperature gradient and producing a front. The opposite process (decreasing the temperature gradient and making the front weaker) is called frontolysis. In chapter 5, the different contributions to frontogenesis are investigated with case and composite studies. The following sections presents the frontogenesis function and the Sawyer–Eliassen equation which describes the circulation at changing fronts (Markowski and Richardson, 2011).

2.9.1 Frontogenesis function

Frontogenesis is described with the frontogenesis function, which is an equation for the total derivative of the magnitude of the potential temperature gradient. The

frontogenesis function is derived by calculating the gradient of the thermodynamic equation as the first step (Yang et al., 2014; Markowski and Richardson, 2011)

$$\frac{\mathrm{d}\theta}{\mathrm{d}t} = \frac{q\theta}{c_p T}, \tag{2.20}$$

where θ is potential temperature, q is diabatic heating rate per unit mass, c_p is specific heat, and T is the actual temperature. The horizontal gradient ∇_H of Equation 2.20 is

$$\begin{aligned}
\nabla_H \left(\frac{\mathrm{d}\theta}{\mathrm{d}t}\right) &= \nabla_H \left(\frac{\partial\theta}{\partial t} + \mathbf{v}\cdot\nabla\theta\right) \\
&= \frac{\partial}{\partial t}\nabla_H\theta + \nabla_H\left(\mathbf{v}\cdot\nabla\theta\right) \\
&= \frac{\mathrm{d}}{\mathrm{d}t}\nabla_H\theta + \nabla_H\mathbf{v}\cdot\nabla\theta \\
&= \nabla_H\frac{q\theta}{c_p T}.
\end{aligned} \tag{2.21}$$

With $\mathbf{v} = (u, v, w)$, the above gives

$$\frac{\mathrm{d}}{\mathrm{d}t}\nabla_H\theta = -\frac{\partial\theta}{\partial x}\nabla_H u - \frac{\partial\theta}{\partial y}\nabla_H v - \frac{\partial\theta}{\partial z}\nabla_H w + \nabla_H\left(\frac{q\theta}{c_p T}\right). \tag{2.22}$$

The frontogenesis function is defined as (Yang et al., 2014; Markowski and Richardson, 2011)

$$\begin{aligned}
F = \frac{\mathrm{d}}{\mathrm{d}t}|\nabla_H\theta| &= \frac{\mathrm{d}}{\mathrm{d}t}\sqrt{\left(\frac{\partial\theta}{\partial x}\right)^2 + \left(\frac{\partial\theta}{\partial y}\right)^2} \\
&= \frac{1}{2|\nabla_H\theta|}\left(2\frac{\partial\theta}{\partial x}\frac{\mathrm{d}}{\mathrm{d}t}\frac{\partial\theta}{\partial x} + 2\frac{\partial\theta}{\partial y}\frac{\mathrm{d}}{\mathrm{d}t}\frac{\partial\theta}{\partial y}\right) \\
&= \frac{1}{|\nabla_H\theta|}\left(\nabla_H\theta\cdot\frac{\mathrm{d}}{\mathrm{d}t}\nabla_H\theta\right).
\end{aligned} \tag{2.23}$$

Inserting for $\frac{\mathrm{d}}{\mathrm{d}t}\nabla_H\theta$ from Equation 2.22 gives

$$\begin{aligned}
F &= \frac{1}{|\nabla_H\theta|}\left(\nabla_H\theta\cdot\left(-\nabla\theta\cdot\nabla_H\mathbf{v} + \nabla_H\frac{q\theta}{c_p T}\right)\right) \\
&= \frac{1}{|\nabla_H\theta|}\left(\nabla_H\theta\cdot\left(-\frac{\partial\theta}{\partial x}\nabla_H u - \frac{\partial\theta}{\partial y}\nabla_H v - \frac{\partial\theta}{\partial z}\nabla_H w + \nabla_H\frac{q\theta}{c_p T}\right)\right) \\
&= \widehat{\nabla_H\theta}\cdot\left(-\frac{\partial\theta}{\partial x}\nabla_H u - \frac{\partial\theta}{\partial y}\nabla_H v - \frac{\partial\theta}{\partial z}\nabla_H w + \nabla_H\frac{q\theta}{c_p T}\right),
\end{aligned} \tag{2.24}$$

where $\widehat{\nabla_H \theta}$ equal to $\nabla_H \theta / |\nabla_H \theta|$ is a unit vector pointing in the same direction as the horizontal potential temperature gradient $\nabla_H \theta$. The terms on the right hand side in Equation 2.24 represent shear (deformation), confluence (divergence or convergence), tilting (frontogenesis or frontolysis due to a horizontal gradient in vertical motion) and differential diabatic heating, respectively. Increasing the potential temperature gradient means that the isentropes are getting tighter. This can be done due to a horizontal gradient in the wind along the front (deformation), by pushing the isentropes together because of a gradient in the wind across the front (convergence), by a gradient in vertical motion (increasing the tilt of the isentropes) or by differential diabatic heating.

2.9.2 Sawyer–Eliassen equation

If the front is changing (intensified or weakened), there is residual ageostrophic circulation. Ageostrophic means not geostrophic, where geostrophic wind means that the wind direction is along isobars (Marshall and Plumb, 2016). The ageostrophic circulation across the front can be investigated using the Sawyer–Eliassen equation. The horizontal wind components u and v are treated as sums of a geostrophic term u_g and v_g and an ageostrophic term u_a and v_a. The Sawyer–Eliassen equation is derived from the semigeostrophic momentum equation in pressure coordinates with the x-axis along the front, e.g., Eliassen (1962), Markowski and Richardson (2011)

$$\frac{\partial u_g}{\partial t} + (u_g + u_a) \frac{\partial u_g}{\partial x} + (v_g + v_a) \frac{\partial u_g}{\partial y} + \omega \frac{\partial u_g}{\partial p} = f_0 v_a, \tag{2.25}$$

and the thermodynamic equation

$$\frac{\mathrm{d}\theta}{\mathrm{d}t} = \frac{\partial \theta}{\partial t} + (u_g + u_a) \frac{\partial \theta}{\partial x} + (v_g + v_a) \frac{\partial \theta}{\partial y} + \omega \frac{\partial \theta}{\partial p} = \frac{q\theta}{c_p T}, \tag{2.26}$$

where a constant Coriolis parameter f_0 is assumed. The Coriolis parameter is a function of latitude, and if the latitude is not changing too much, this is a reasonable assumption. ω is the vertical velocity expressed in Pascal per second, Pa s^{-1}. The reason why Equation 2.25 and Equation 2.26 are expressed in pressure coordinates and not height coordinates is because the thermal wind relations are used in the derivation. The thermal wind relations have a simpler expression in pressure coordinates than in height coordinates. Constant Coriolis parameter means non-divergent geostrophic flow, i.e., $\frac{\partial u_g}{\partial x} = -\frac{\partial v_g}{\partial y}$. u_g is the geostrophic wind along the front and it is not changing locally, i.e., $\frac{\partial u_g}{\partial t} = 0$. The coordinate system is chosen so that the x-axis is parallel to the front and the y-axis points towards

the cold air. u_a is equal to 0 because the ageostrophic circulation is confined to the yp-plane. Assuming non-divergent ageostrophic circulation, a stream function ψ may be defined

$$v_a = -\frac{\partial \psi}{\partial p}, \quad \omega = \frac{\partial \psi}{\partial y}. \tag{2.27}$$

The thermal wind relations in pressure coordinates are

$$\frac{\partial \theta}{\partial x} = -\frac{f_0 p}{R}\frac{\theta}{T}\frac{\partial v_g}{\partial p}, \quad \frac{\partial \theta}{\partial y} = \frac{f_0 p}{R}\frac{\theta}{T}\frac{\partial u_g}{\partial p}. \tag{2.28}$$

Thermal wind is a vertical difference in geostrophic wind (Marshall and Plumb, 2016; Cushman-Roisin and Beckers, 2011). Subtracting $\frac{RT}{f_0 p\theta}\frac{\partial}{\partial y}$ (2.26) from $\frac{\partial}{\partial p}$ (2.25) and inserting for the stream function and the thermal wind relations gives the Sawyer–Eliassen equation

$$\begin{aligned} -\frac{RT}{f_0 p\theta}\frac{\partial \theta}{\partial p}\frac{\partial^2 \psi}{\partial y^2} - 2\frac{\partial u_g}{\partial p}\frac{\partial^2 \psi}{\partial p \partial y} + \left(f_0 - \frac{\partial u_g}{\partial y}\right)\frac{\partial^2 \psi}{\partial p^2} \\ = 2\frac{RT}{f_0 p\theta}\left(\frac{\partial u_g}{\partial y}\frac{\partial \theta}{\partial x} + \frac{\partial v_g}{\partial y}\frac{\partial \theta}{\partial y}\right) - \frac{R}{c_p f_0 p}\frac{\partial q}{\partial y}, \end{aligned} \tag{2.29}$$

where horizontal variations of static stability are neglected since $\frac{\partial^2 u_g}{\partial p^2}$ is proportional to $\frac{\partial}{\partial y}\left(\frac{\partial \theta}{\partial p}\right)$, which is equal to 0. It is also assumed that $\frac{\partial}{\partial y}\left(\frac{\partial u_g}{\partial p}\right) \propto \frac{\partial^2 \theta}{\partial y^2} = 0$, which means the strength of the baroclinity is a constant within the frontal zone (Markowski and Richardson, 2011).

The terms on the left hand side in Equation 2.29 represent static stability, horizontal temperature gradient through thermal wind and inertial instability, respectively. On the right hand side the terms represent frontogenetical forcing by geostrophic wind and differential diabatic heating. According to Markowski and Richardson (2011), cold fronts often have stronger circulations than warm fronts, as well as sharper temperature gradients, because the deformation terms on the right hand side in Equation 2.29 are often frontogenetic.

Equation 2.29 is a linear second order partial differential equation, and can be solved numerically or analytically using Green's functions (see for instance Zauderer (2011) or Økland (1998)). In this thesis the total frontogenesis (the sum of the four terms in Equation 2.24) is used to approximate the overturning circulation, and hence the stream function, described by the Sawyer–Eliassen equation (Equation 2.29). The shape of the stream function is controlled by the magnitude of the coefficients in Equation 2.29. The eccentricity if the circulation is controlled by

the relative strength of the static stability compared with the inertial instability (Markowski and Richardson, 2011).

The reader interested in the dynamics of fronts is referred to Markowski and Richardson (2011) or Lin (2007). In chapter 5, the frontogenetical forcing on CAOs are investigated through case and composite studies.

2.10 Vertical averaging

The potential temperature tendencies are vertically averaged and plotted on a map in chapter 3 and chapter 4. In the following, it is explained how the averaging is performed. From to 1000 to 750 hPa there exists values of diabatic temperature tendencies with an increment of 25 hPa. These values are used in the averaging. The diabatic temperature tendencies are calculated using ERA Interim. The data are accumulated temperature tendencies around the specific time step, 00:00, 06:00, 12:00 and 18:00. For the 00:00 and the 12:00 hour time steps the heating is only accumulated 3 hours prior to the time step. This means that, for example, for 00:00 the heating is accumulated between 21:00 and 00:00. For these time steps the heating is multiplied by two to get the same units (K per 6 hours). What is calculated is the *temperature* tendency, $\frac{\mathrm{d}T}{\mathrm{d}t}$. The *potential temperature* tendency, $\frac{\mathrm{d}\theta}{\mathrm{d}t}$ at some pressure level p is

$$\frac{\mathrm{d}\theta}{\mathrm{d}t} = \frac{\mathrm{d}T}{\mathrm{d}t}\left(\frac{p_0}{p}\right)^{R/c_p}, \tag{2.30}$$

which is similar to the definition of the potential temperature in Equation 2.1. The vertically averaged diabatic heating in a certain grid point is defined as

$$\overline{\frac{\mathrm{d}\theta}{\mathrm{d}t}} = \frac{1}{\mathrm{d}p_{total}}\int_{p_s}^{750\ hPa}\frac{\mathrm{d}\theta}{\mathrm{d}t}\mathrm{d}p \approx \frac{1}{\mathrm{d}p_{total}}\sum_i\left(\frac{\mathrm{d}\theta}{\mathrm{d}t}\right)_i \mathrm{d}p_i, \tag{2.31}$$

where $\frac{\mathrm{d}\theta}{\mathrm{d}t}$ is the potential temperature tendency, p_s is the surface pressure and $\mathrm{d}p_{total}$ is the pressure difference between the surface pressure and 750 hPa. Equation 2.31 gives a mean diabatic heating rate in the vertical. The heating rate at some pressure level p is assumed to be representative in the interval p + 12.5 hPa and p - 12.5 hPa. $\mathrm{d}p_i$ is the pressure difference between two neighbor pressure levels. If the surface pressure in a certain grid point is greater than 1000 hPa, for example 1005 hPa, then $\mathrm{d}p_1$ is equal to 5 hPa + 12.5 hPa = 17.5 hPa. $\mathrm{d}p_2$ is then equal to 25 hPa as the heating rate at 975 hPa is assumed to be representative between 962.5 hPa and 987.5 hPa and so on. If the surface pressure is less than 1000 hPa,

dp is set to NaN. The vertically averaged heating rate is not defined (it is set to NaN) in grid points where the surface pressure is less than 750 hPa.

Chapter 3

Case studies

In this chapter, two selected CAOs are studied in detail, one in the Fram Strait in the period December 23–27, 2015 and another one in the Barents Sea in the period January 11–20, 2015. The events are chosen from the time series of the mean CAO index inside each of the regions shown in Figure 1.1, and the entire region shown on the maps is investigated. The synoptic conditions (MSLP, potential temperature at 900 hPa and geopotential height), heat fluxes and the vertically averaged potential temperature tendencies are investigated and compared during the two CAOs. In chapter 5 the frontogenesis at the onset of the CAOs is investigated and compared to the composites.

When the CAOs to study were chosen, it was ensured that the duration was not too long. For CAOs that last for 20–30 days or longer, it might be more reasonable to treat them as several short-lived events rather than one very long-lived event. The two CAOs chosen for the case studies last for less than ten days.

3.1 Case study of a CAO in the Fram Strait

The first CAO to be studied in this chapter is an event occurring in the Fram Strait in the period December 23–27, 2015. It is the fourth event that occurred in the Fram Strait during the winter 2015/2016 (Figure 2.1). The onset time step is December 23, 00:00 and the end time step is December 27, 18:00, according to the threshold determined in section 2.5. This event has a duration of five days and the maximum mean CAO index inside the box is 13.2 K, according to the running mean (Figure 3.1). Figure 3.1 shows the time series defining this event (the running mean) and the original time series. There is one peak in the running

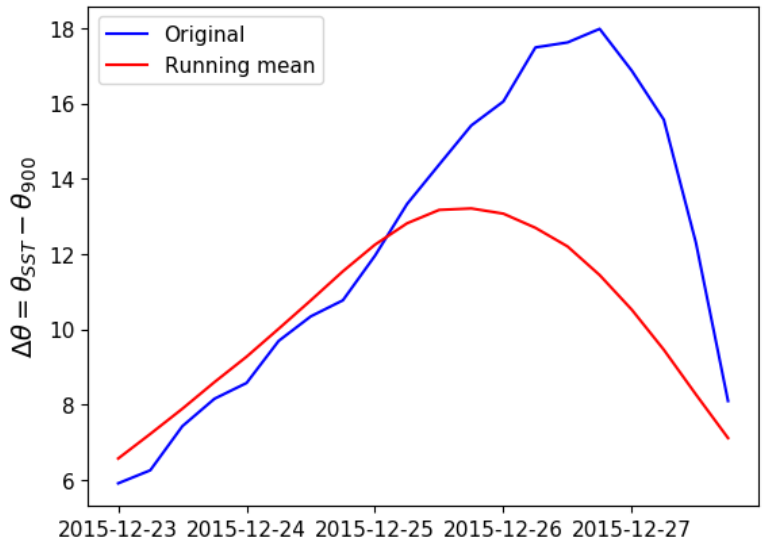

Figure 3.1: Timeseries of the mean CAO index in Fram Strait for December 23 to December 27, 2015. The red line shows the running mean, and the blue line shows the original timeseries.

mean, occurring at December 25, 18:00, which means that there was only one pulse of cold air. In the following, a few selected time steps during the CAO are described and discussed.

3.1.1 December 23, 18:00

December 23, 18:00 is 18 hours after the onset of the event. The synoptic conditions at this time step are shown in Figure 3.2a and Figure 3.2b. There is a cyclone at the surface east of Iceland (Figure 3.2a). Also at 900 hPa there is a cyclone approximately at the same location (contours in Figure 3.2b). The cyclone is progressing northeastwards during the following time and it is sitting in the Barents Sea when the CAO in the Fram Strait is intensified, as seen in the next time steps investigated.

The geostrophic wind at 900 hPa is from the north through the Fram Strait (Figure 3.2b). At this time step the wind is not very intense, because the lines of constant Z500 are not very tight. There is a surface cyclone sitting north of Novaya Zemlya (Figure 3.2a). The Z500 contours in the same figure show a cyclone located northwest of the surface cyclone, which indicates that there is baroclinic growth (Eady, 1949; Vallis, 2017). This goes along with the potential temperature gradient in the Barents Sea (Figure 3.2b) because baroclinic instability occurs due

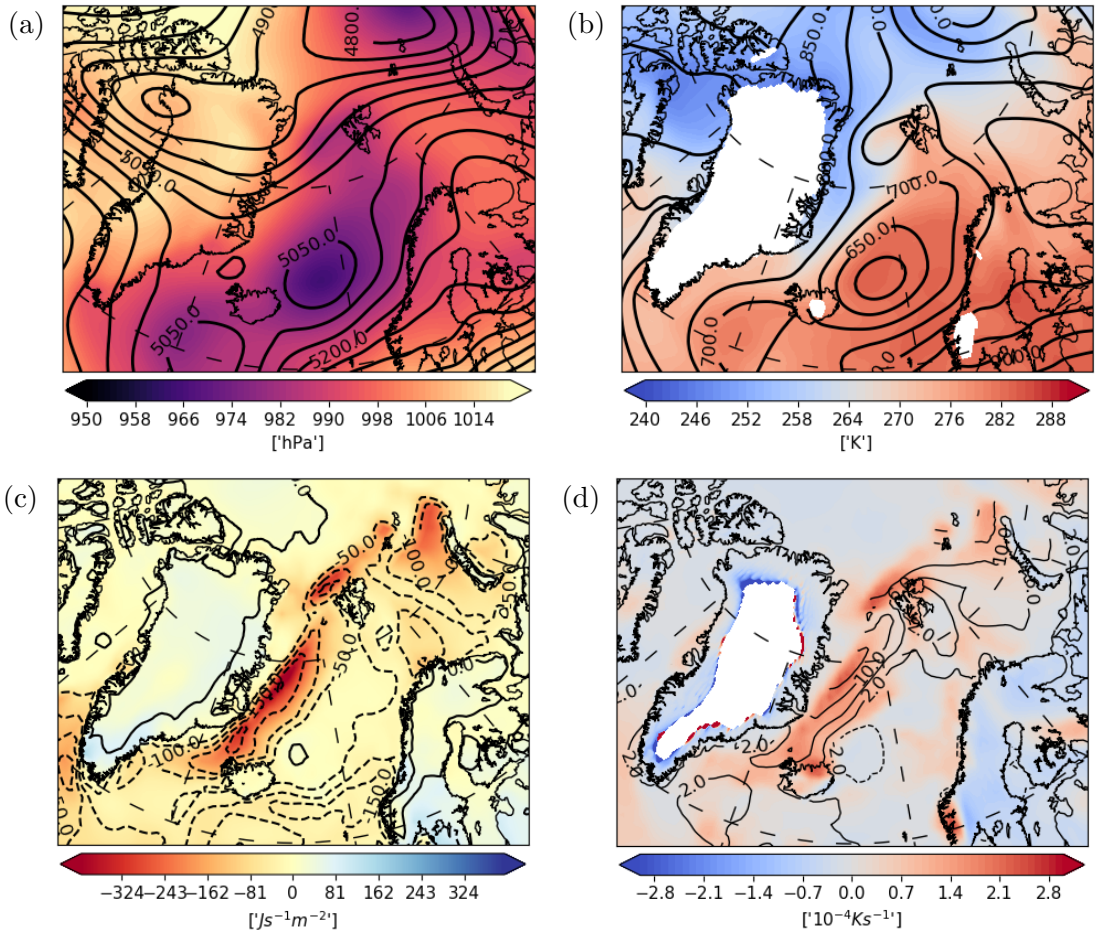

Figure 3.2: (a) MSLP (hPa; shading) and geopotential height at 500 hPa (Z500) (m; contours), (b) potential temperature at 900 hPa (K; shading) and geopotential height at 900 hPa (Z900) (m; contours), (c) Surface sensible (shading) and latent (contours) heat fluxes in Wm^{-2}, (d) vertically averaged potential temperature tendency (10^{-4} Ks^{-1}; shading) and CAO index (K; contours) at December 23, 18:00.

to a horizontal temperature gradient (Vallis, 2017). In addition, there is a trough over Novaya Zemlya in the Z500 contours (Figure 3.2a). This trough is also seen in the Z900 (contours in Figure 3.2b). Over Northern Scandinavia there is a ridge in the Z500 contours (Figure 3.2a). At the surface there is a cyclone sitting north of Novaya Zemlya (Figure 3.2a) and at 500 hPa there is a cyclone northwest of Novaya Zemlya, which indicates that there is a baroclinic growth there as well as closer to the Fram Strait.

In Figure 3.2c and Figure 3.2d, the heat fluxes and vertically averaged heating rates are shown. From the CAO index (contours in Figure 3.2d) it is possible to tell roughly where the ice edge is, because the CAOs index is only defined in grid points where there is sea, and where the sea ice cover is less than 0.5. This can also be seen from the heat fluxes (Figure 3.2c). No latent heat flux indicates that there is ice or land in these grid points.

Because of the large sensible heat flux (Figure 3.2c) and the CAO index of 10 K south of the Fram Strait, it seems like there is an event in the East Greenland box as well. In fact, this is the case. A CAO is detected outside East Greenland in the period December 22, 00:00 to December 26, 18:00. This CAO is associated with northerlies. Cold air is advected from the north through the Fram Strait, causing large CAO index in the East Greenland box as well. It is very likely the same CAO, with advection of cold air masses through both boxes.

From the sensible heat flux and the CAO index in the north of the Barents Sea (Figure 3.2c and Figure 3.2d), it seems like there could be a CAO there at the same time as there was a CAO in the Fram Strait. However, no events in the Barents Sea are detected in this period. The mean CAO index in this area is actually above the threshold, but the running mean is not (not shown). Thus, there is likely a CAO here, but it has not been detected by the procedure used in this thesis for detecting events. It could have been detected a CAO in this region with a smaller latitude-longitude box than that shown in Figure 1.1. If the grid points containing low CAO indices were excluded, the mean CAO index would be larger. This is not further investigated. However, if there was a CAO in the Barents Sea, it was short lived according to the time series of the mean CAO index there (not shown). The time series of the mean CAO index in the Barents Sea during the end of December 2015 (not shown) shows that there likely was two CAOs in this area during the period December 23–28, although they are not detected by the procedure used in this work. The original time series was well above the threshold, but the running mean was not. There is no formal mathematical definition of a CAO, so these events could have been detected as CAOs with a different procedure.

3.1.2 December 24, 18:00

At this time step the potential temperature field shows that the cold air has progressed southwards through the Fram Strait (Figure 3.3b). There is a cyclone sitting over Svalbard, advecting cold air from the north. The cyclone has progressed from the southeast compared with the previous time step. At 500 hPa the geostrophic wind is coming from the west over Greenland and turning to northeast in the Fram Strait (Figure 3.3a). This seen in context with Figure 3.3b implies

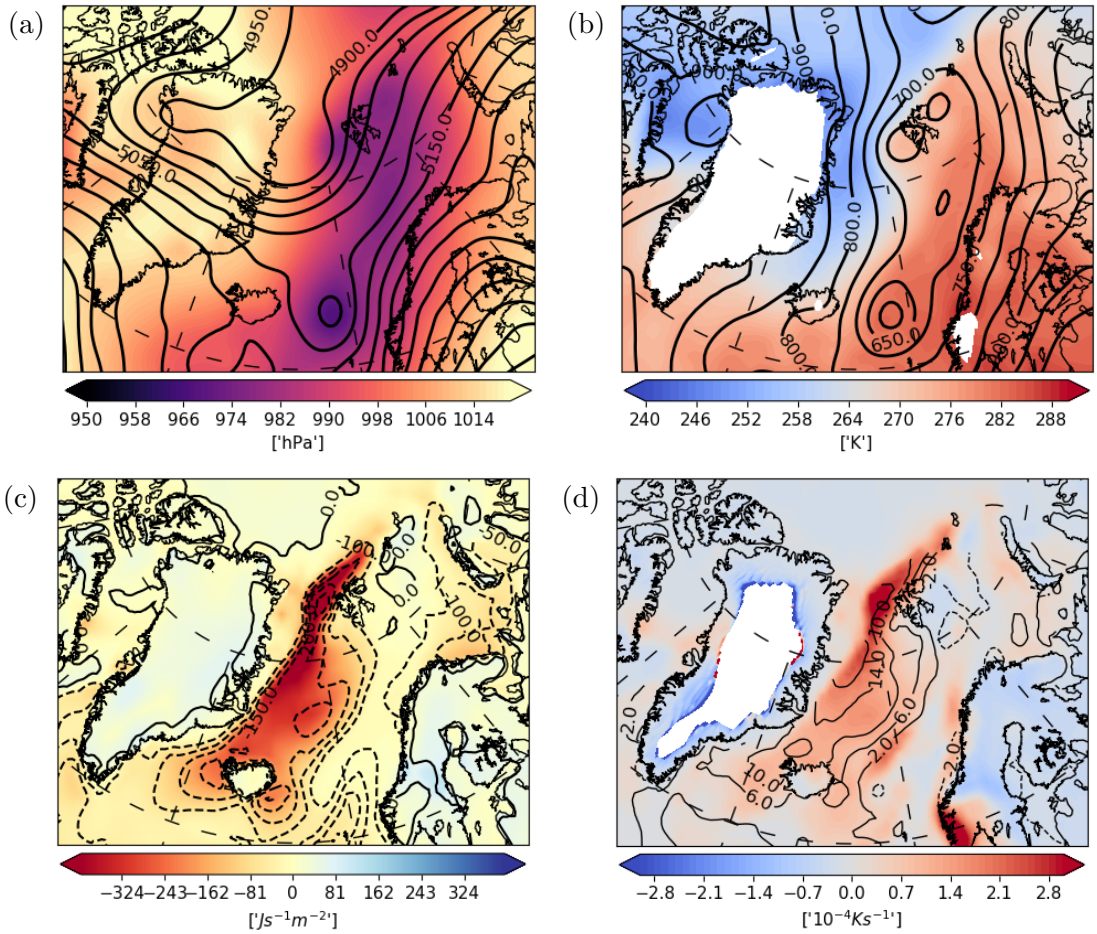

Figure 3.3: Same as Figure 3.2, but for December 24, 18:00.

that the geostrophic wind is turning anticlockwise with height. The thermal wind vector (difference in geostrophic wind between two pressure levels) has a direction along the potential temperature contours, with cold air to the left on the northern hemisphere. Anticlockwise turning with height is called backing (Markowski and Richardson, 2011)[1], and implies cold air advection. The geostrophic wind at 900 hPa is intensified from the previous time step (Figure 3.2b, Figure 3.3b). Now the wind is clearly from the north trough the Fram Strait.

The heat fluxes and heating rates are intensified (Figure 3.3c and Figure 3.3d) at this time step. The CAO index (Figure 3.3d) is 10–14 K in the Fram Strait region. According to Figure 3.3c, this CAO is affecting the heat flux in a large part of the Norwegian Sea. The sensible heat flux is largest close to the ice edge ($\approx$ 400 Wm^{-2}). The latent heat flux is around 150–200 Wm^{-2}. In Figure 3.3d,

[1]The opposite phenomenon, clockwise turning in wind direction with height is called veering.

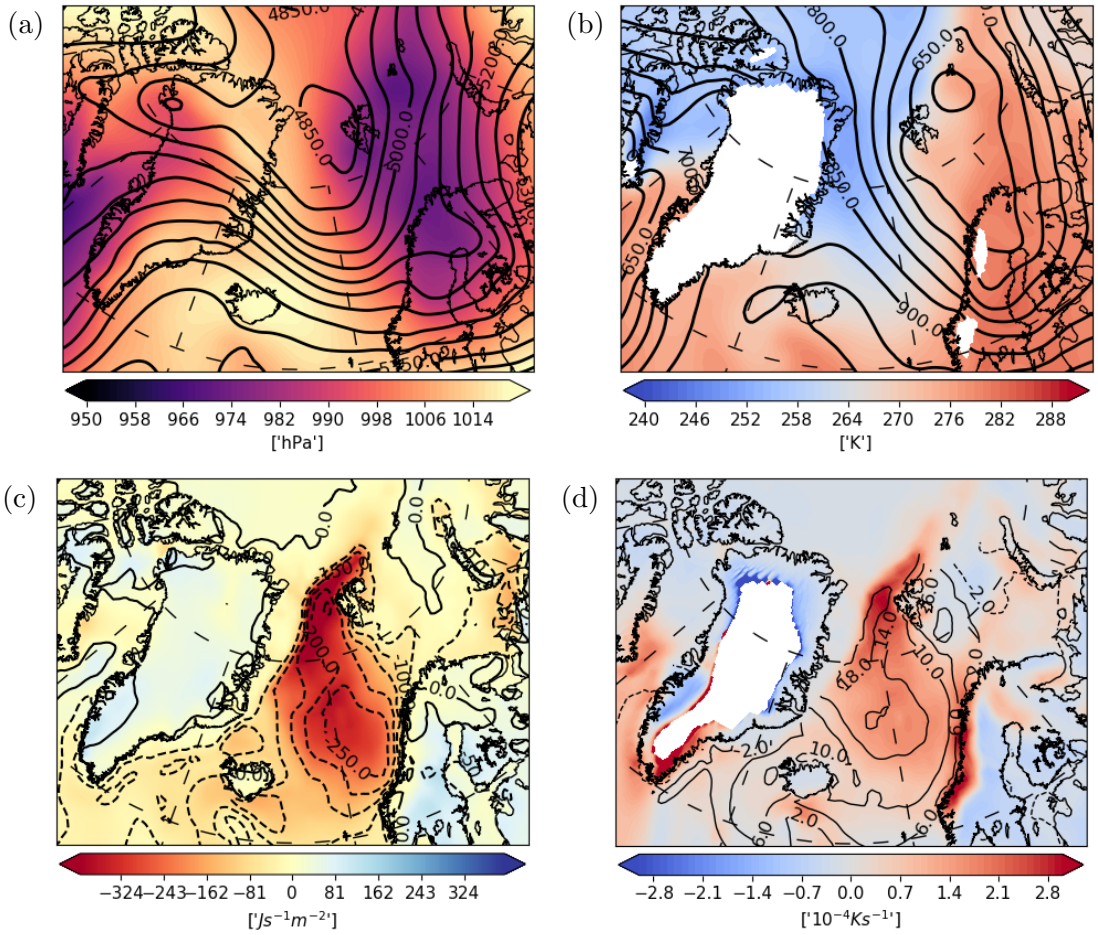

Figure 3.4: Same as Figure 3.2, but for December 25, 18:00.

the vertically averaged potential temperature tendency is shown together with the CAO index. The northern part of the Fram Strait has the largest heating rate, approximately $3 \cdot 10^{-4}$ Ks^{-1}. In the Barents Sea the heating rate and the CAO index are close to 0. Also the sensible heat flux in this area has decreased rapidly.

3.1.3 December 25, 18:00

This is the peak time step according to the running mean in Figure 3.1. According to the MSLP and Z500 fields (Figure 3.4a), there is a westward tilt with height, meaning that the upper level cyclone is sitting west of the surface cyclone. This indicates that there is baroclinic growth, as in Figure 3.2a. The result goes along with Mansfield (1974), who showed that there is a relation between CAOs and baroclinic instability. From the lines of constant Z900 (Figure 3.4b), it is clear that

this is an event associated with northerlies. The geostrophic wind turns eastwards and hits the Norwegian coast. One could imagine that the event could be detected in this region as well. This is not the case (not shown), probably because the event is not vigorous enough. There are some contours of high CAO index outside the Norwegian coast (Figure 3.4d), but there are not enough grid points with large enough CAO index so that the mean CAO index exceeds the threshold. It might have been detected a CAO in this region if the box was smaller (not investigated). The Norwegian coast box could have been shrink in the south. In this way several grid points with low CAO index values would have been excluded from the mean, which would give a larger mean CAO index inside the box.

The sensible heat flux has decreased a little at this time step (Figure 3.4c), and the latent heat flux has increased. Now the latent heat flux is 100–200 Wm^{-2}. The area with large sensible heat flux relative to the surroundings has moved towards the east. In this area the potential temperature tendency is also larger than the surroundings (Figure 3.4d).

3.1.4 December 26, 18:00

One day before the event ends, the potential temperature at 900 hPa in the southern part of the map has increased (Figure 3.5b), probably because of the large heat fluxes during the event. At 500 hPa there is a well pronounced trough from Svalbard and southeast to Scandinavia (Figure 3.5a). Also at 900 hPa there is a trough (Figure 3.5b). There is still a westward tilt with height, hence baroclinic growth in the northern part of the map. Furthermore, the potential temperature at 900 hPa field shows a zonal temperature gradient west of Svalbard (Figure 3.5b). The geostrophic wind has turned from northerlies at the previous time step to northwesterlies.

The surface sensible heat flux has decreased (Figure 3.5c), and the area with strong sensible heat flux has moved further towards the east from the previous time step. This can be seen in context with the geostrophic wind direction at 500 and 900 hPa (Figure 3.5a, Figure 3.5b), which is from the northwest. As in the previous time step, there are large heat fluxes outside the coast of Northern Norway. In the Norwegian coast box defined in Figure 1.1, there are grid points with large CAO indices (Figure 3.5d), but not large enough to detect a CAO there. The intensity of the event has decreased considerable, which can be seen both from the time series (Figure 3.1) and the CAO index contours in Figure 3.5d.

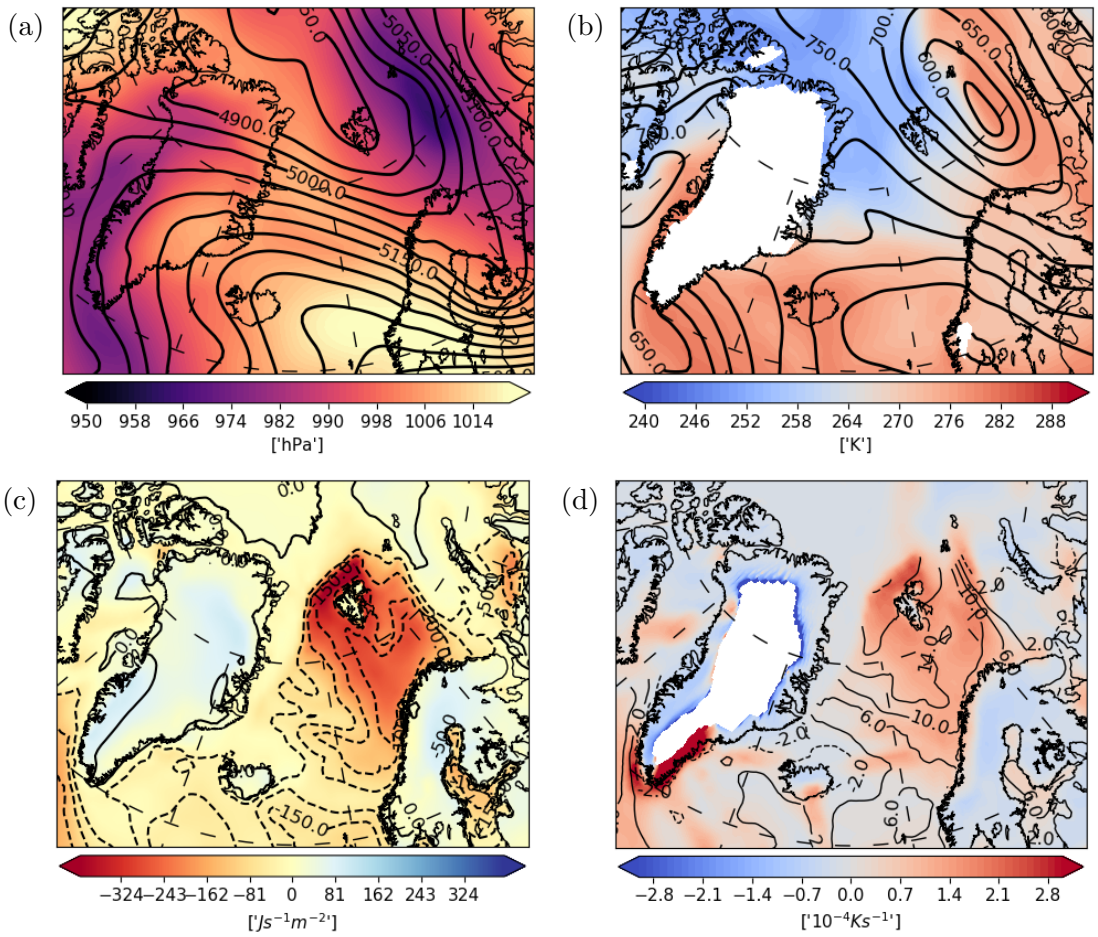

Figure 3.5: Same as Figure 3.2, but for December 26, 18:00.

3.2 Case study of a CAO in the Barents Sea

The second event to be studied is a CAO that occurred in the Barents Sea in January 2015. The onset of this event is January 11, 18:00, and the end time step is January 20, 12:00. This event has the largest peak in the running mean at January 17, 18:00. Figure 3.6 shows the time series of the event. This event has three peaks with respect to the running mean that defines it, which indicates that there are three pulses of cold air. The running mean is not dropping very much after the first and the second peak, so it makes sense to treat this as one event and not split into more separate events. The peaks occur at January 14, 18:00, January 17, 18:00 (the largest peak) and January 19, 12:00. In this section the onset and the peaks of the event are studied.

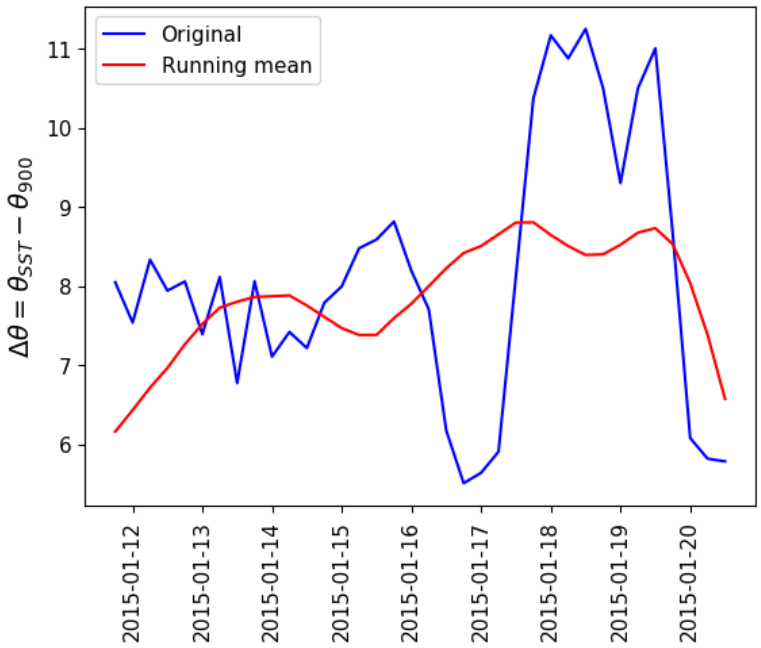

Figure 3.6: Time series defining a CAO in the Barents Sea in the period January 11–20, 2015. The blue line is the original time series, and the red line is the running mean.

3.2.1 January 11, 18:00

This is the onset time step of the event. At this time step there is a cyclone sitting in the lower left corner of the map, southeast of Greenland (Figure 3.7a, Figure 3.7b). This cyclone is progressing northeastwards, towards the Barents Sea. There is also a trough over Iceland. At 900 hPa there is an anticyclone sitting west of Svalbard (Figure 3.7b), producing geostrophic easterlies in the Barents Sea. There is a cold air mass sitting over Novaya Zemlya (Figure 3.7b).

The sensible heat flux is negative west of Novaya Zemlya (Figure 3.7c), which means that the surface is losing heat to the atmosphere. The sensible heat flux is largest close to Novaya Zemlya ($\approx$ 150–160 Wm^{-2}), and it is larger than the latent heat flux of approximately 50–100 Wm^{-2}. This event has a low heating rate ($\approx$ 0.5–1 $\cdot 10^{-4}$ Ks^{-1}) at the onset compared to the event in the previous case study (Figure 3.2c). There is an area outside Northern Norway where the sensible heat flux is as large as in the Barents Sea (Figure 3.7c). There is a short lived and not so intense event going on in this region. It could be the same event as that in the Barents Sea. It is clear that the potential temperature in Northern Norway is lower than in the Norwegian Sea (Figure 3.7b), and the geostrophic wind is from

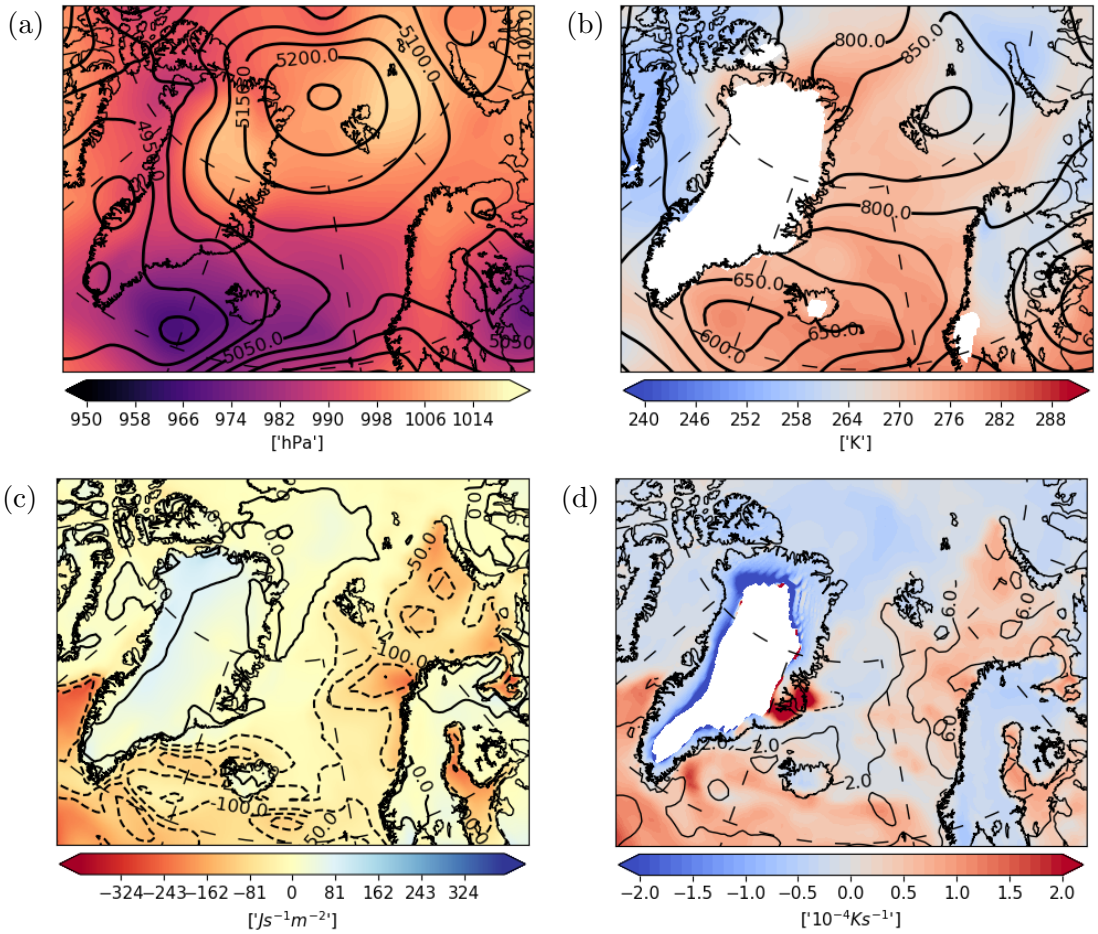

Figure 3.7: Same as Figure 3.2, but for January 11, 18:00.

the east. The thermal wind vector is pointing southwards along the Norwegian coast, implying anticlockwise turning (backing) and advection of cold air.

3.2.2 January 14, 06:00

At this time step, the first peak occurs. The cyclone that was located south of Greenland at the onset (Figure 3.7a, Figure 3.7b) is now located west of Northern Norway (Figure 3.8a, Figure 3.8b). There is a cyclone at 900 hPa sitting west of Norway, giving geostrophic wind from the east in the Barents Sea. The lines of constant Z500 indicates that the geostrophic wind in the Barents Sea is not very strong. Over Northern Greenland there is an anticyclone with a ridge towards the south (Figure 3.8a). This anticyclone was also seen in Figure 3.7a. At this time step the anticyclone has mowed towards the west.

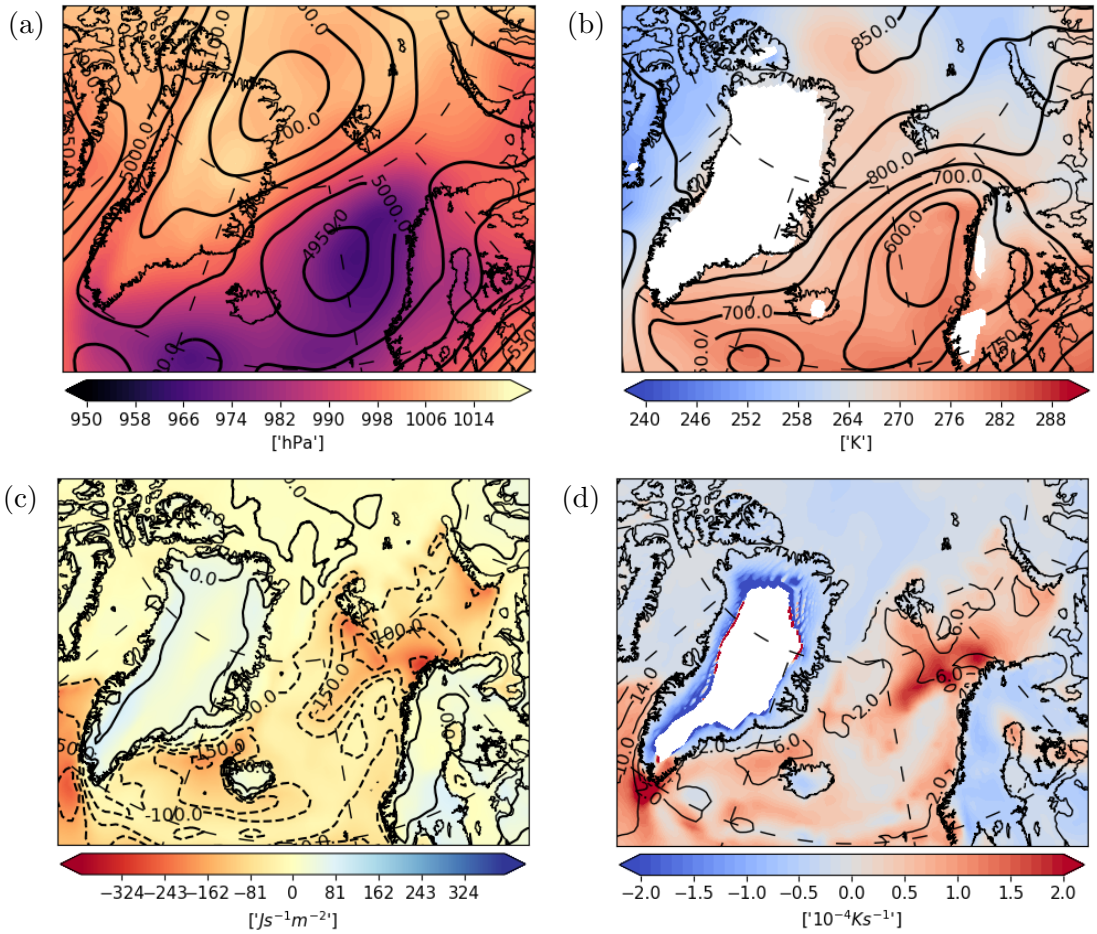

Figure 3.8: Same as Figure 3.2, but for January 14, 06:00.

There are large values of heat fluxes and diabatic heating along the coast of Finnmark in Northern Norway (Figure 3.8c and Figure 3.8d). This indicates that the cold air from east of Novaya Zemlya is advected westwards. The mean CAO index outside the Norwegian coast is below the threshold at this time step, but if the latitude-longitude box in Figure 1.1 was made smaller, a CAO might have been detected here.

3.2.3 January 17, 18:00

This is the largest peak of the event. There is a weak surface cyclone sitting in the south of the Barents Sea (Figure 3.9a), compared to the surface cyclone during the CAO in the Fram Strait studied in section 3.1. Over Greenland the MSLP is high, larger than 1014 hPa. The westward tilt is less pronounced in this case

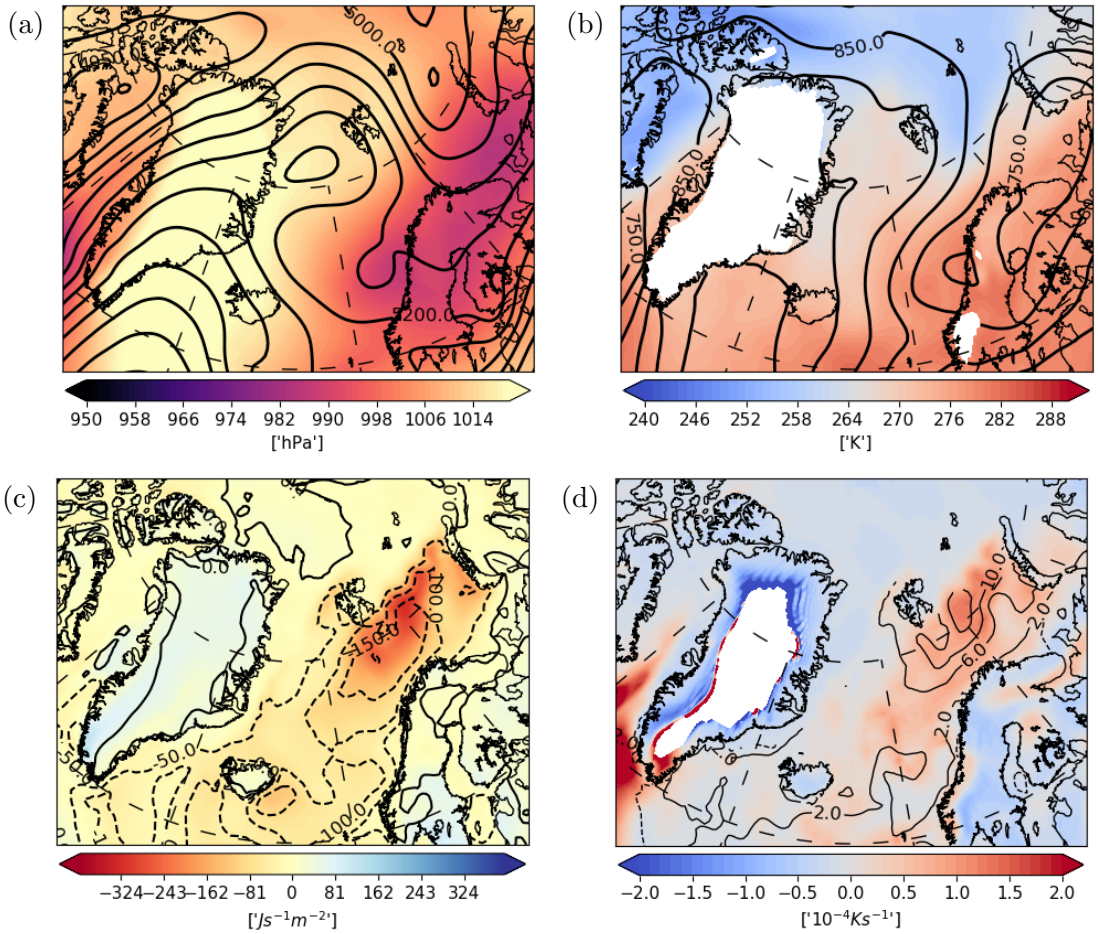

Figure 3.9: Same as Figure 3.2, but for January 17, 18:00.

than in the previous case (Figure 3.4a). At 500 hPa there is a ridge north of the Fram Strait and a trough in the Barents Sea (Figure 3.9a). From Figure 3.9b it can be seen that the geostrophic wind is from the northeast. In a region southeast of Svalbard the surface sensible heat flux is large compared to the surroundings (Figure 3.9c). From the CAO index (contours in Figure 3.9d) it is clear that this event is less intense than the previous one. This can also be seen from the time series defining the two events (Figure 3.1, Figure 3.6). The CAO index is around 10 K inside the box covering the Barents Sea (Figure 1.1). The region with large heat fluxes and diabatic heating is extended towards the west from the previous time steps, indicating that the cold air is advected in this direction (Figure 3.9c, Figure 3.9d).

3.2.4 January 19, 12:00

The last peak occurred on this time step. This is one day before the end of the event. Now, the MSLP is larger than 1014 hPa over a large part of the region shown in the map (Figure 3.10a). There is a cyclone sitting east of Novaya Zemlya, and the geostrophic wind at 500 hPa is from the northeast. Over Northern Greenland there is a ridge. At 900 hPa the wind is predominantly from the north (Figure 3.10b). The Z500 contours (Figure 3.10a) show a ridge over Greenland and a trough over Western Russia. Southwest of Iceland there is a cyclone (Figure 3.10a, Figure 3.10b). There is no tilt with height, indicating that the atmosphere is barotropic at this location.

The surface sensible heat flux in the Barents Sea region is large ($\approx$ 200 Wm^{-2}), and the latent heat flux is around 100 Wm^{-2} (Figure 3.10c). The area with large heat flux ($\geq$ 400 Wm^{-2}) has moved towards the east from the previous time step. This indicates that the cold air is advected southeastwards, which goes along with the geopotential height contours in Figure 3.5a and Figure 3.5b. There are grid points with large CAO index, although the mean CAO index in the Fram Strait is just above the threshold of 6.1 K. Both events are associated with troughs and ridges, which goes along with the already established knowledge about the synoptic conditions during CAOs.

3.3 Summary and comparison

To summarize this chapter, two CAOs in the Fram Strait and in the Barents Sea are investigated. The CAO in the Fram Strait was the most intense one and had the shortest duration. In the Barents Sea there was three peaks during the event, whereas the Fram Strait event only had one peak in the running mean. At the onset there was geostrophic wind from the north at 900 hPa in the Fram Strait, indicating that the cold air is advected southwards. The event in the Barents Sea had geostrophic wind from the east at the onset, which means that it is associated with easterlies according to the separation procedure explained in section 2.6. During the event in the Fram Strait there was two pulses of cold air in the Barents Sea. These are not detected as CAOs because the mean CAO index in this region increased rapidly so that the running mean never exceeded the threshold.

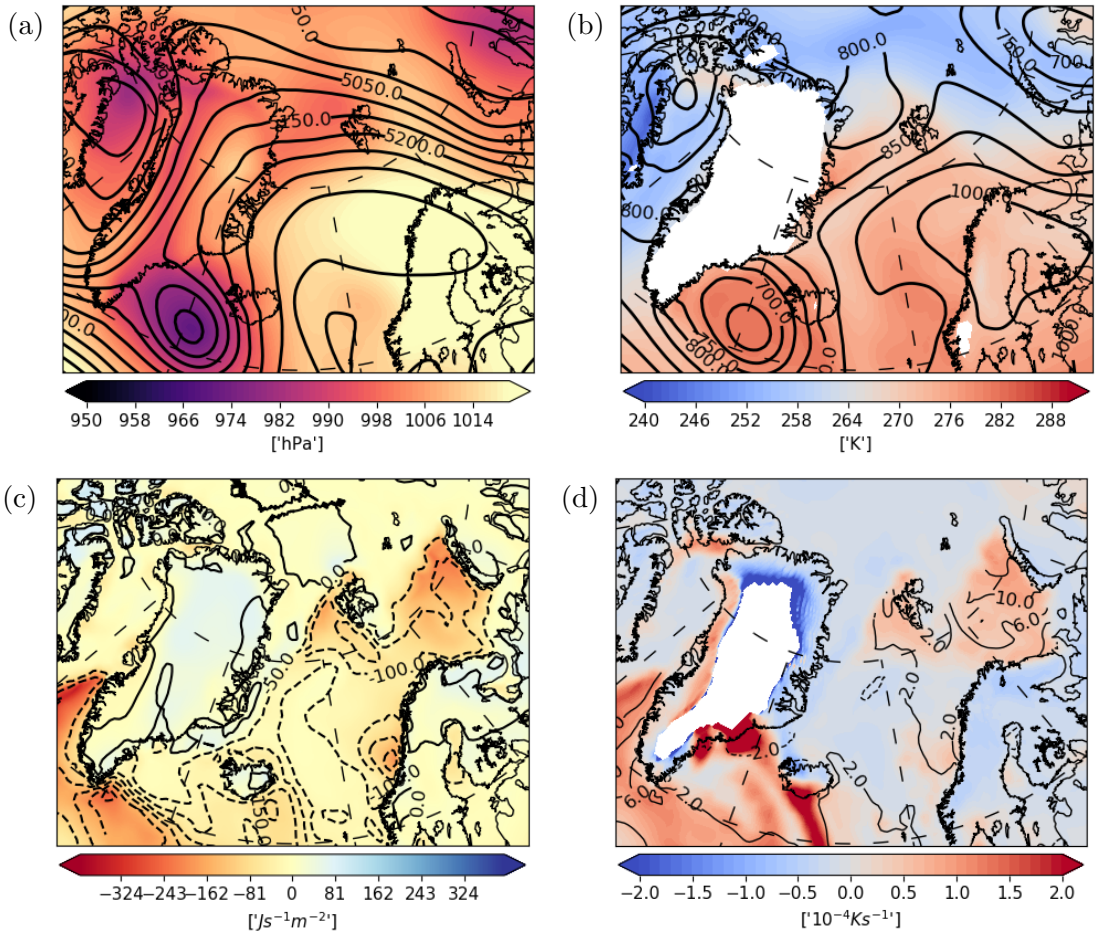

Figure 3.10: Same as Figure 3.2, but for January 19, 12:00.

Chapter 4

Composites

The composites are calculated based on the onset and the maximum CAO index time steps, with lags ± 72 hours and an increment of 12 hours. Here, only the onset and the maximum CAO index time steps are shown. The first section describes some of the properties of the events. Next, the composites are presented, first those based on the onset time steps, and then those based on the maximum CAO index time steps. This is followed by a section on composite standard deviations. In the last section a significance test on the MSLP composites is performed and the result is discussed.

4.1 Duration and intensity

CAOs are detected in ERA Interim using the time series analysis described in section 2.5 and the separation method described in section 2.6. The composites in each box are calculated for each wind direction. This is done to detect CAOs associated with other wind directions. Composites of the wind at 900 hPa based on all CAOs inside a certain region would only show northerlies in the region.

	North	South	East	West	Total
Fram Strait	250	7	21	44	322
Barents Sea	168	17	73	20	278
East Greenland	197	5	10	17	229
Norwegian coast	107	4	40	28	179

Table 4.1: Number of events in the different boxes associated with the different wind directions a the time steps with maximum CAO index during 1979–2016.

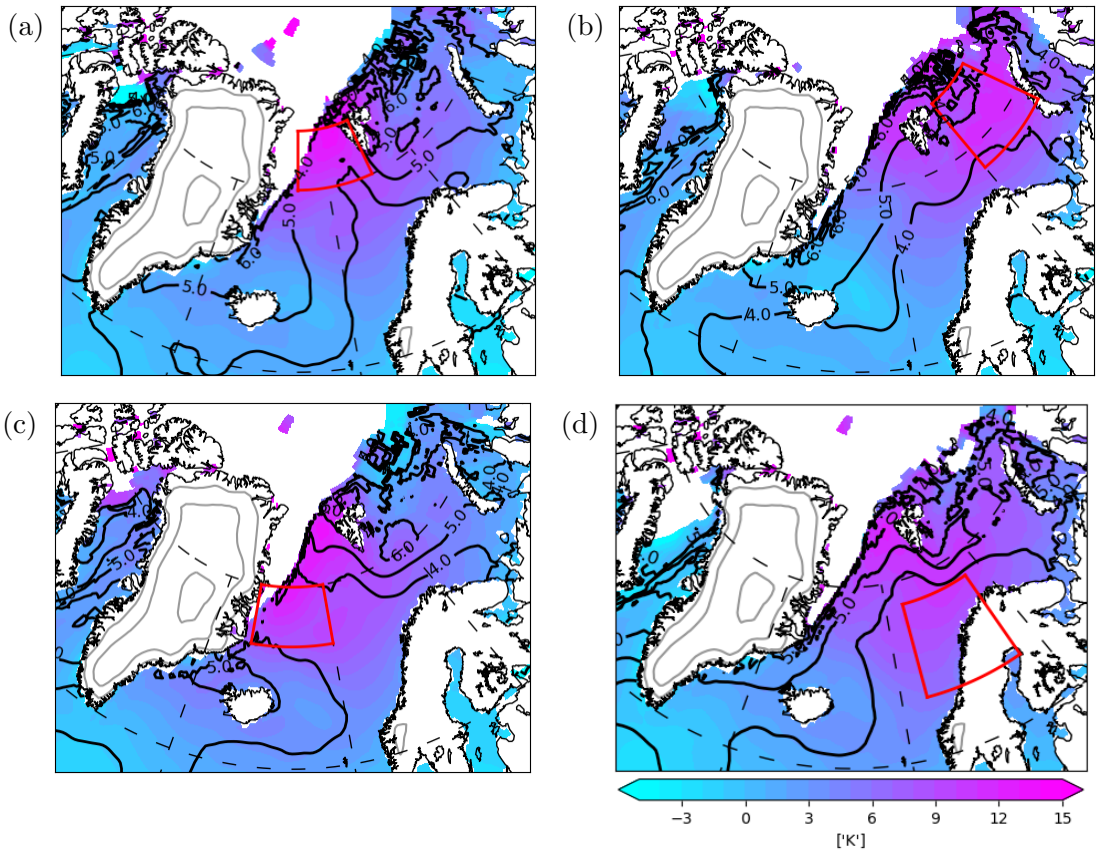

Figure 4.1: Composites of the CAO index (K; shading) and standard deviations (K; contours) in (a) the Fram Strait, (b) the Barents Sea, (c) East Greenland and (d) the Norwegian coast. The composites are based on the maximum CAO index time steps.

With the separation method it is possible to detect CAOs associated with other wind directions.

Table 4.1 shows the number of events associated with the different wind directions. Most CAOs are associated with northerlies at the maximum CAO index time steps. Some of the events outside East Greenland are detected in the Fram Strait as well. This goes along with the fact that cold air masses are advected from the north both through the Fram Strait and the East Greenland box south of the Fram Strait box. 17 of the maximum CAO index time steps in the Fram Strait also occur in the East Greenland box.

The distribution of the events is as expected. When a CAO starts, the cold air masses must come from places producing cold air, for example from the sea ice or from land areas containing cold air. For the Fram Strait it is expected advection of

	Fram Strait	Barents Sea	East Gr.land	Norw. coast
Fram Strait	-	250	219	174
Barents Sea	-	-	148	146
East Gr.land	-	-	-	136

Table 4.2: Number of CAOs occurring in two or more boxes at the same time.

Fram Str., East Gr.land, Bar. Sea	37
Fram Str., East Gr.land, Norw. coast	28
Fram Str,. Bar. Sea, Norw. coast	33
Bar. Sea, East Gr.land, Norw. coast	3

Table 4.3: Number of cases where there are CAOs at the same time in three boxes according to the definition of CAOs used in this thesis. There are 107 cases where there are CAOs in all four boxes at the same time. This number is subtracted from the number of CAOs in three boxes at the same time.

cold air from the sea ice in the north and from Greenland in the west. This is also the case for the East Greenland box further south. Regarding the Barents Sea box it is expected cold air masses from the sea ice in the north, as in the Fram Strait. In addition there could be cold air advection from Novaya Zemlya in the east. This goes along with the fact that more events in the Barents Sea are associated with easterlies than westerlies. In the Barents Sea and the Norwegian coast box there are more CAOs from the east than from the west. Both the Fram Strait and East Greenland have more CAOs from the west than from the east. CAOs from the east in the Fram Strait and East Greenland and CAOs from the west in Barents Sea are likely air masses from Svalbard. Thus, CAOs with wind from Svalbard at the maximum CAO index time steps are less common than CAOs with wind from Greenland or from Novaya Zemlya. For the Norwegian coast there is a possibility that there could be CAOs from the Norwegian mainland, but also in this box CAOs associated with northerlies are most common. Several of these events, or maybe all of them, are most likely the same events as those in the Barents Sea or in the Fram Strait, i.e., the cold air is advected from the ice until it reaches the Norwegian coast box.

For each of the boxes a list of CAO dates is produced. Then the lists of dates for the boxes are compared in order to check whether the same dates occur in two or more lists. Table 4.3 shows the number of coinciding CAOs in three boxes. There are most coinciding events in the Fram Strait, East Greenland and the Barents Sea (37 events). The Barents Sea, East Greenland and the Norwegian coast is the group of boxes with fewest coinciding events, only 3. This means that there are rarely CAOs in all boxes except from the Fram Strait.

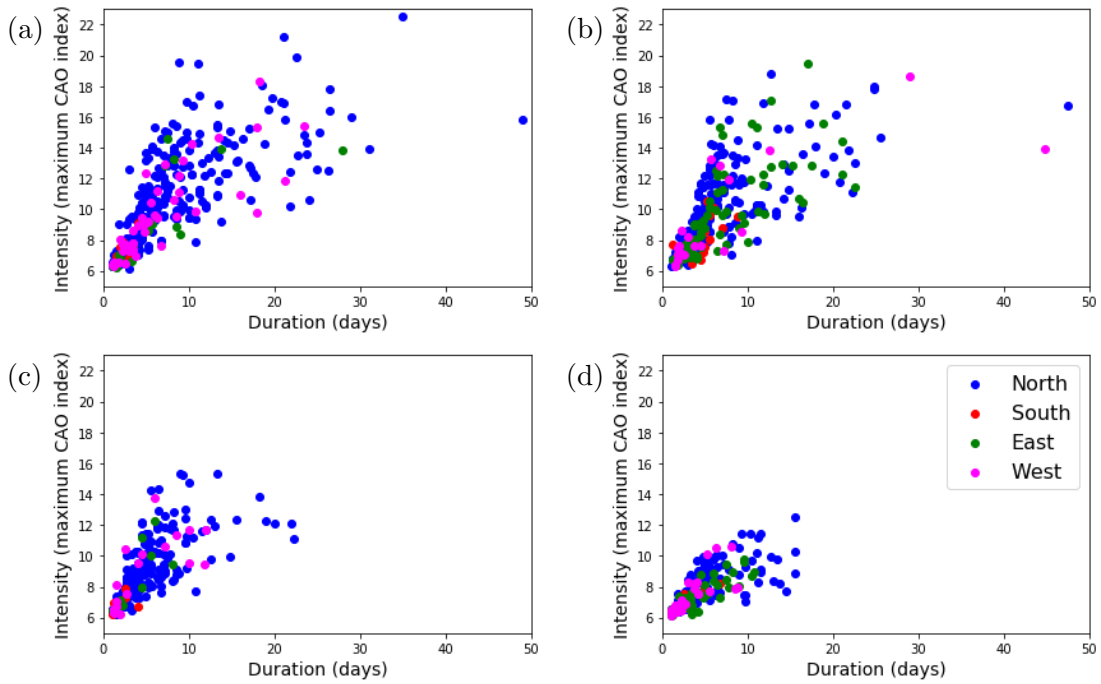

Figure 4.2: Relation between the duration (days; horizontal axis) and the intensity (maximum CAO index within each event according to the running mean time series) of the events associated with the different wind directions in (a) the Fram Strait, (b) the Barents Sea, (c) East Greenland and (d) the Norwegian coast.

In Figure 4.1 composites of the CAO index are shown. Here the events are not separated with respect to the wind direction. When the CAO index is large outside East Greenland, it is also large in the Fram Strait (Figure 4.1c). This indicates that a large part of the events detected outside East Greenland are detected in the Fram Strait as well, as shown in Table 4.2. The composites based on CAOs outside the Norwegian coast (Figure 4.1d) show that when the CAO index is large in this region, it is large in the Fram Strait as well. Also in the Barents Sea region there are large values, approximately 10–12 K. This indicates that CAOs outside the Norwegian coast are most likely advection of cold air from the Fram Strait or the Barents Sea. In addition, the composite standard deviation of the CAO index is shown as contours in Figure 4.1. The contours show standard deviations of 4–5 K. For CAOs in East Greenland (Figure 4.1c) the standard deviation is 14 K in some grid points. The large composite standard deviations of the CAO index indicate that the intensity of CAOs vary a lot from event to event. The composite standard deviations of the MSLP and the potential temperature at 900 hPa are discussed in section 4.4.

The duration of an event is defined as the time it takes for the mean CAO index to exceed the threshold and drop below the threshold again (see section 2.3 and section 2.5). Intensity can be measured in different ways, for example by the mean CAO index within the event, the sum of all CAO indices during the event or the largest local maximum (the largest peak). Figure 4.2 show scatter plots with duration in days on the horizontal axis and intensity (maximum CAO index within the event, the largest peak) on the vertical axis. The most intense and long lived events are associated with wind from the north. A few events are associated with wind predominantly from the south. These events are short lived and not very intense. The fact that the wind direction at the peak time step is from the south does not necessarily mean that there is advection of cold air from the south. It could also be the case that the wind direction is turning during the events. This might also be the case for events associated with easterlies and westerlies. To answer the question of where the cold air is actually coming from, it would be necessary to do a trajectory analysis (Papritz and Spengler, 2017).

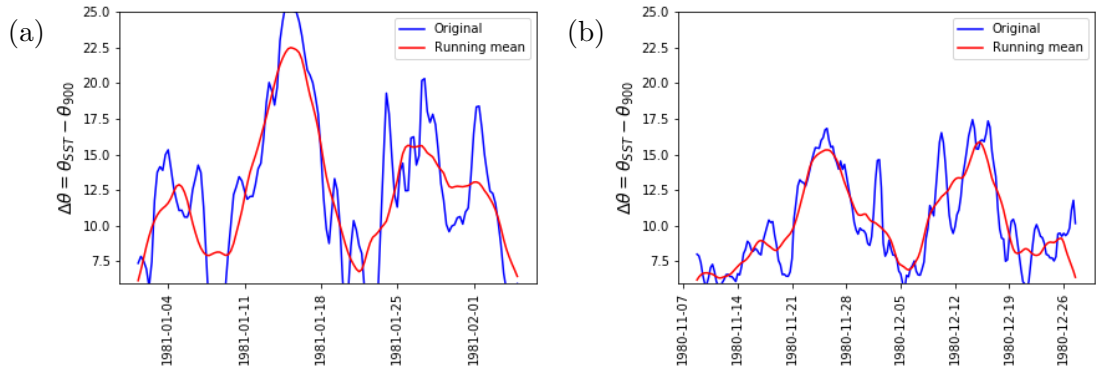

Figure 4.3: Examples of CAOs in the Fram Strait with duration longer than 30 days. The blue line is the original time series, and the red line is the running mean.

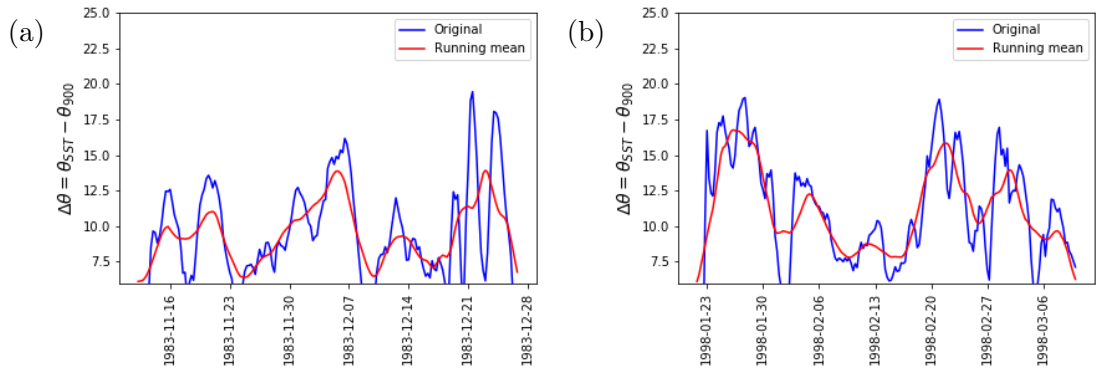

Figure 4.4: Same as Figure 4.3, but for the Barents Sea.

A few events have a duration of one month or longer. These events consist of several pulses of cold air, mainly from the north. Most of the long lived events would be split into two or more events with a slightly larger threshold $\Delta\theta_{thresh}$ (explained in section 2.5). In Figure 4.3, the time series of two long lived events (duration longer than 30 days) in the Fram Strait are shown. According to the scatter plot (Figure 4.2a), there is one event lasting for 50 days. The time series of this event is shown in Figure 4.3b. The Barents Sea also has some long lived events. Two of these are shown in Figure 4.4. In the scatter plot (Figure 4.2b) it is shown that there are two events that last for more than 40 days. The time series of these events are shown in Figure 4.4a and Figure 4.4b. The events that have the longest duration are characterized by pulses of cold air and several local maxima in the time series (Table 4.4).

	Number of local maxima								
	1	2	3	4	5	6	7	8	9
Fram Strait	193	64	36	11	12	2	2	1	1
Barents Sea	174	56	22	13	2	7	3	1	
East Greenland	162	42	14	7	2	1	1		
Norwegian coast	127	23	14	10	3	1	1		

Table 4.4: Number of events with number of local maxima in the running mean timeseries.

Most events have just one local maximum (Table 4.4), but in the Fram Strait and the Barents Sea there are some events with several local maxima. The reason is that the running mean time series still contain some short term fluctuations. Although there are events with several local maxima, these events may contain only two or three peaks. Also, the events with several local maxima are typically those with long duration (Figure 4.3, Figure 4.4).

In addition to the composites based on the peaks in the time series, it is also useful to look at composites based on the onset time steps. These composites give an indication of what is going on at the beginning of a CAO. Furthermore, the lagged composites based on the peaks will not cover the onset time steps for the long lived events.

4.2 Composites based on the onset time steps

The synoptic conditions at the onset of CAOs in the different regions and for different wind directions are compared and interpreted physically. Only the Fram

Strait, the Barents Sea and the Norwegian coast boxes are investigated in the following as the situation during CAOs in the East Greenland box are similar to the Fram Strait box.

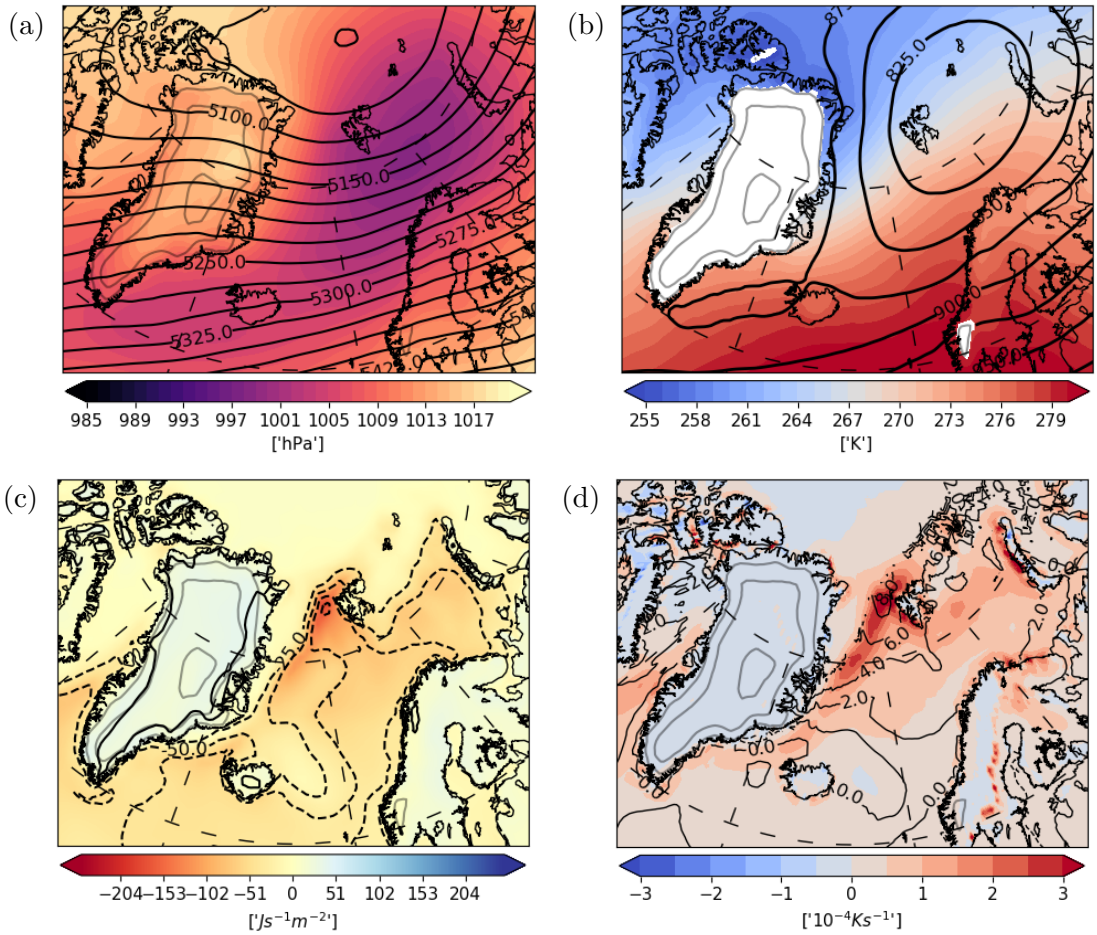

Figure 4.5: Composites based on the onset time steps of (a) MSLP (hPa; shading) and Z500 (m; contours), (b) potential temperature at 900 hPa (K; shading) and Z900 (m; contours), (c) sensible (shading) and latent heat flux (contours) in Wm^{-2} and (d) vertically averaged potential temperature tendency (Ks^{-1}; shading) and CAO index (K; contours) for CAOs in the Fram Strait associated with northerlies.

4.2.1 Fram Strait

At the onset of CAOs in the Fram Strait, only events associated with northerlies are shown at the onset. The composites based on the onset time steps for CAOs in

the Fram Strait associated with northerlies and westerlies are very similar. In Figure 4.5, the synoptic conditions at the onset of CAOs associated with northerlies are shown. According to the MSLP (Figure 4.5a), there is a cyclone sitting southwest of Svalbard, advecting cold air southwards through the Fram Strait. The contours of the Z900 show that there is geostrophic wind from the north through the Fram Strait, with a cyclone sitting in the Barents Sea. As in the case study, the thermal wind vector according to the potential temperature at 900 hPa (shading in Figure 4.5b) points towards the northeast. This means that the geostrophic wind is turning anticlockwise with height, consistent with cold air advection. The center in the cyclones at sea level and at 500 hPa (Figure 4.5a) show a northwestward tilt with height. This means that there is a baroclinic growth, as in the case study of the CAO in the Fram Strait.

Wacker et al. (2005) did a case study on a CAO in the Fram Strait occurring in April 4–6, 1998. From the procedure of detecting CAO presented in section 2.6, this event is associated with wind from the north. The event had a synoptic situation consistent with the composites, with a high over Greenland and a low over the Barents Sea.

Also the heat fluxes and the heating rates are similar for CAOs associated with northerlies and westerlies. These values are shown only for events associated with northerlies (Figure 4.5c, Figure 4.5d). The surface sensible heat flux in the Fram Strait is around 150 Wm^{-2} and a latent heat flux of around 50 Wm^{-2} (Figure 4.5c). The vertically averaged potential temperature tendency is around $3 \cdot 10^{-4}$ Ks^{-1} inside the Fram Strait region (Figure 4.5d), and it is large compared to the surroundings. The CAO index is approximately 6 K inside the Fram Strait region (Figure 4.5d). Both groups of CAOs (northerlies and westerlies) contain some intense events and some less intense events (Figure 4.2a). These less intense events contribute to a low composite value of the CAO index.

In Figure 4.6 the mean Z500 over a box covering Northern Greenland is plotted against the mean Z500 over a box covering Svalbard. It is expected that the mean Z500 decreases over Svalbard and increases over Northern Greenland at the onset of a CAO. This is a case for some of the events shown in Figure 4.6, but not for all. The events shown in magenta and green shows a decrease over Svalbard and an increase over Northern Greenland after the onset. For the event shown in black there is in fact an increase over Svalbard and minor changes over Northern Greenland. The event shown in purple shows decrease both over Svalbard and Norther Greenland before the onset, but after the onset there is an increase over Northern Greenland.

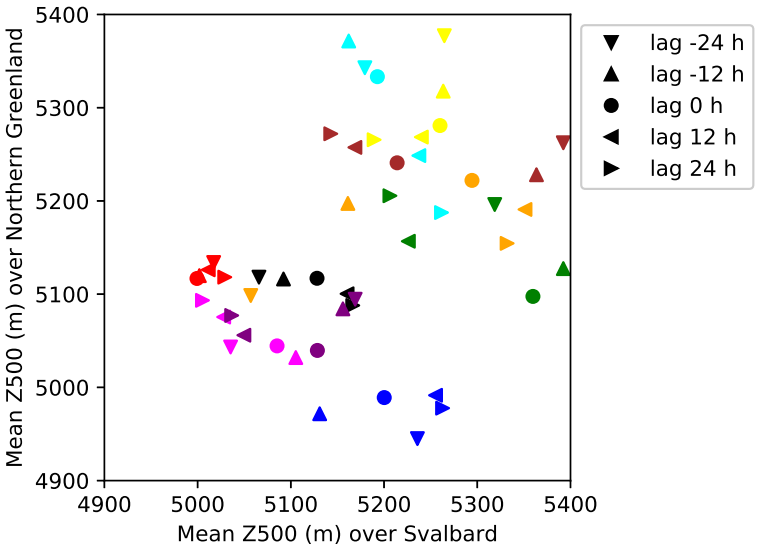

Figure 4.6: Relation between the spatial mean Z500 in meters in a box over Northern Greenland and a box over Svalbard for the ten most intense CAOs in the Fram Strait. Lag 0 h is the onset time steps of the CAOs. Each color corresponds to one event. The most intense event is shown in red, and the next colors are, in descending order: blue, green, magenta, yellow, cyan, black, purple, orange and brown.

4.2.2 Barents Sea

For the Barents Sea, only CAOs with easterlies at the maximum CAO index time steps are discussed. The events associated with northerlies are very similar to those in the Fram Strait, with a cyclone sitting over Novaya Zemlya and advecting cold air towards the south (not shown).

During the events in the Barents Sea associated with easterlies, there is a surface cyclone sitting outside the coast of northern Norway (Figure 4.7a). The upper level cyclone shown with contours of Z500 is located east of Novaya Zemlya. In this configuration there is not a well pronounced westward tilt with height as is expected when there is baroclinic growth. There is a well defined ridge at the eastern coast of Greenland. The contours of Z900 (Figure 4.7b) shows that there is geostrophic wind predominantly from the east, indicating that the cold air is coming from the east. These contours also indicate that there is a trough over the Norwegian Sea and a ridge northwest of Svalbard.

The surface sensible heat flux west of Novaya Zemlya is approximately 140 Wm^{-2} (Figure 4.7c), and the latent heat flux is around 50 Wm^{-2}. In this region the

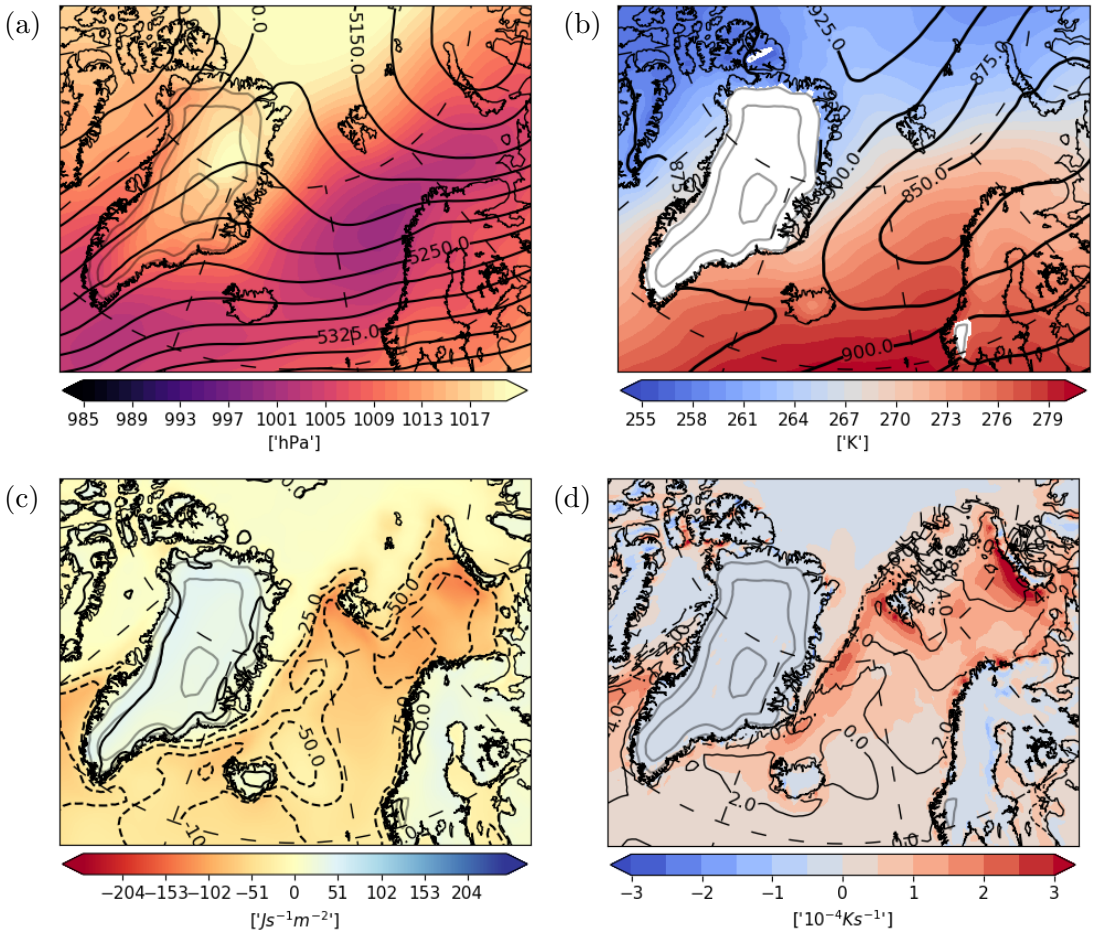

Figure 4.7: Same as Figure 4.5, but for events in the Barents Sea associated with easterlies.

potential temperature tendency is large compared to the rest of the map, approximately $3 \cdot 10^{-4}$ Ks^{-1}. There is also an area west of Svalbard where the vertically averaged potential temperature tendency is large. The CAO index is large in the north of the Barents Sea region ($\approx$ 8 K) and low further south ($\approx$ 4 K). Most of the 73 events in the Barents Sea associated with easterlies are not very intense (maximum CAO index less than 10 K) according to the scatter plot in Figure 4.2b.

4.2.3 Norwegian coast

For the Norwegian coast it was hypothesized that there could be CAOs from the Norwegian mainland, i.e., from the east, from the south or from the southeast. In Figure 4.8 composites based on events associated with easterlies are shown. The

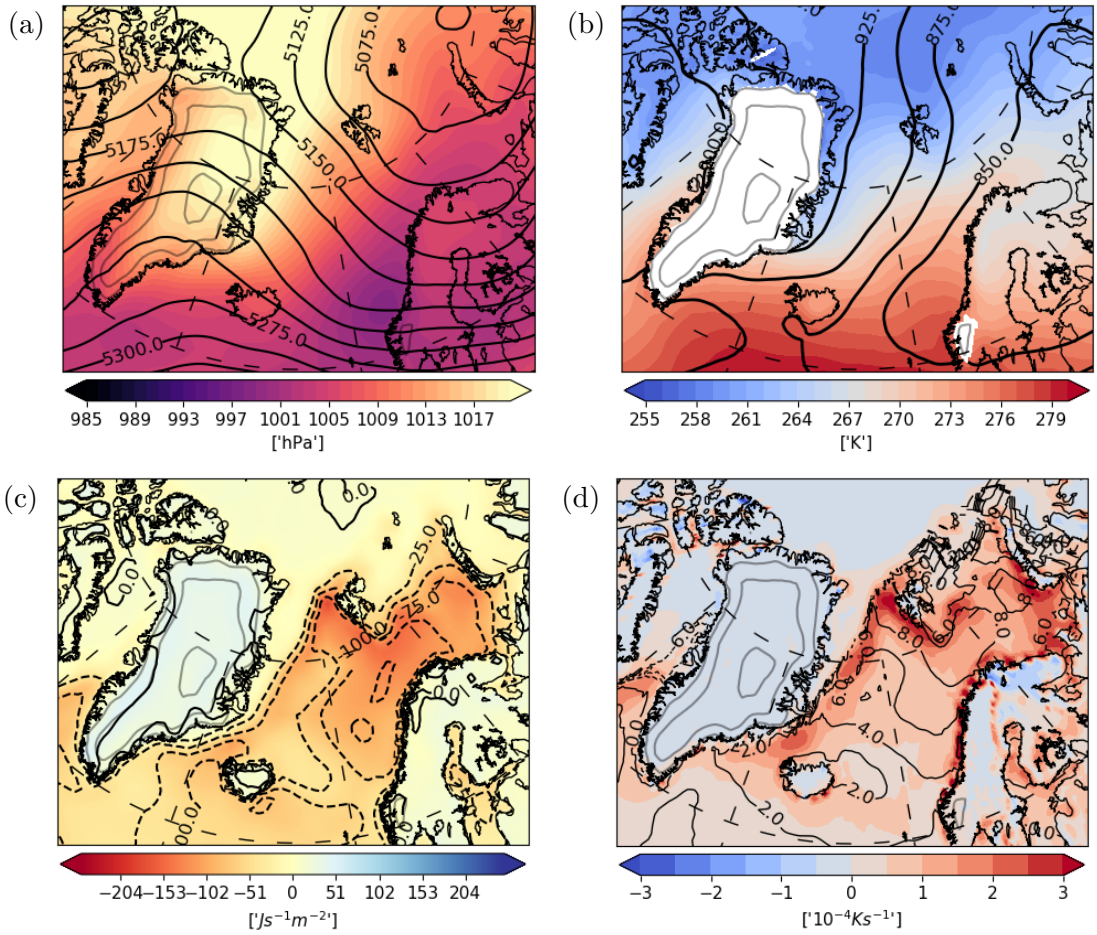

Figure 4.8: Same as Figure 4.5, but for CAOs outside the Norwegian coast associated with easterlies.

composites based on events with southerlies are not shown because there are only seven of these (Table 4.1). It is not so useful to look at composites with only a few members because these composites are not very representative. The contours of Z500 show a cyclone located northeast of Novaya Zemlya (Figure 4.8a). Looking at the potential temperature at 900 hPa and Z900 (Figure 4.8b), the geostrophic wind is from the northeast. It is likely that some of these events are the same as those in the Barents Sea. However, the potential temperature in Northern Norway is slightly lower than in the sea. It is likely that this relatively colder air is advected by the large scale wind.

The heat fluxes are shown in Figure 4.8c. As for the other configurations, the sensible heat flux is larger than the latent heat flux. The sensible heat flux is largest in the Fram Strait and southeast of Svalbard, approximately 150 Wm^{-2}.

The vertically averaged potential temperature tendency (Figure 4.8d) is large in the Fram Strait and west of Novaya Zemlya compared to the surroundings. Also close to the Norwegian coast there are large values. Regarding the CAO index (contours in Figure 4.8d) this variable is 6–8 K inside the Norwegian coast box defined in Figure 1.1. This goes along with the fact that the CAOs outside the Norwegian coast associated with easterlies are not very intense compared to CAOs in the Fram Strait and in the Barents Sea.

4.3 Composites based on the peak time steps

This section presents the composites based on the largest peak within the time series of each event. These composites give an indication of what is the typical synoptic situation when a CAO is on its most intense stage.

4.3.1 Fram Strait

The synoptic conditions for events in the Fram Strait associated with northerlies are shown in Figure 4.9. Looking at MSLP and Z500 (Figure 4.9a), there is a well defined westward tilt with height east of Svalbard, indicating a baroclinic growth (Eady, 1949; Vallis, 2017). In addition there is a trough over Northern Greenland. The tilt is less defined in the case with westerlies (Figure 4.10), but also in this case there is a trough over Northern Greenland. Regarding the potential temperature fields (Figure 4.9b and Figure 4.10b), there is not a big difference. The Z900 contours, on the other hand are different. In the case with northerlies (Figure 4.9b), there is a cyclone sitting in the Barents Sea, east of Svalbard, advecting cold air southwards. The other case (Figure 4.10b) is showing a cyclone sitting north of Svalbard, advecting cold air from Greenland in the west. Looking at the lagged composites of the Z900 based on the peak time steps for CAOs in the Fram Strait associated with westerlies (not shown), the geostrophic wind turns towards westerlies as the peak time step is approaching. 48 hours before the peak the wind is predominantly from the north through the Fram Strait. At lag -24 hours, 24 hours before the peak, the wind is from the northwest. After this the wind turns towards easterlies as the peak is approaching. Both cases have a thermal wind vector pointing northeastwards, indicating backing, which means advection of cold air.

In Figure 4.11, the relation between the mean Z500 over a box covering Greenland and a box covering Svalbard is shown. The composites indicate that the points should lie in the upper left triangle of the figure. This means that when the Z500 is

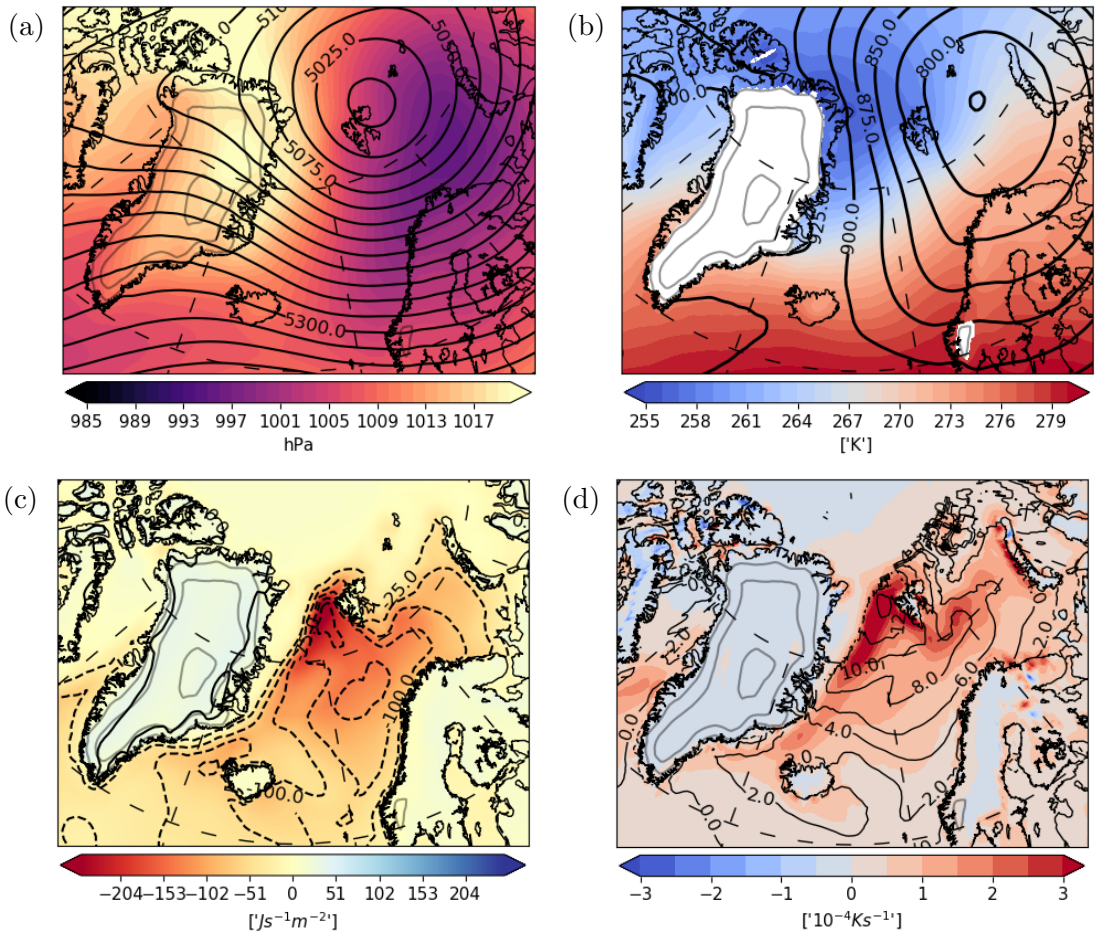

Figure 4.9: Same as Figure 4.5, but for the peak time steps.

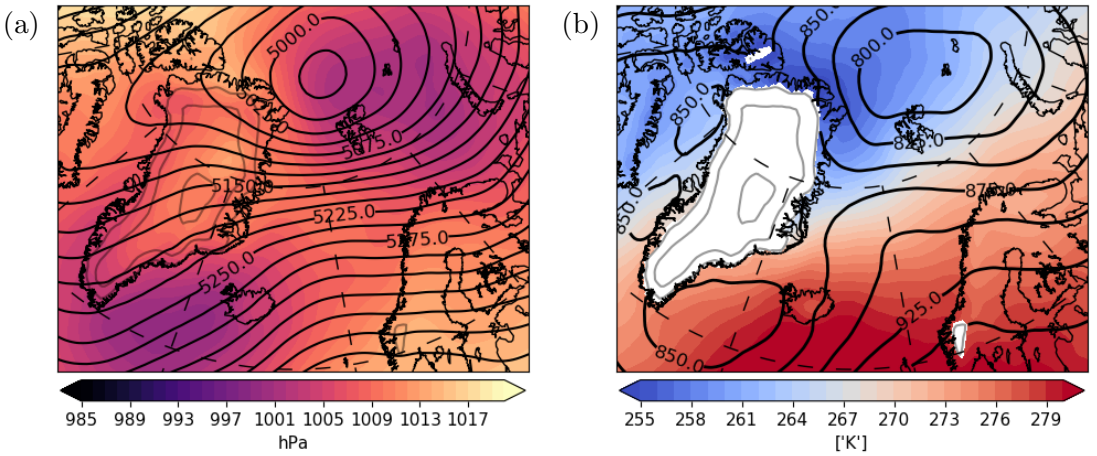

Figure 4.10: Same as Figure 4.5, but for the peak time steps and for events associated with westerlies.

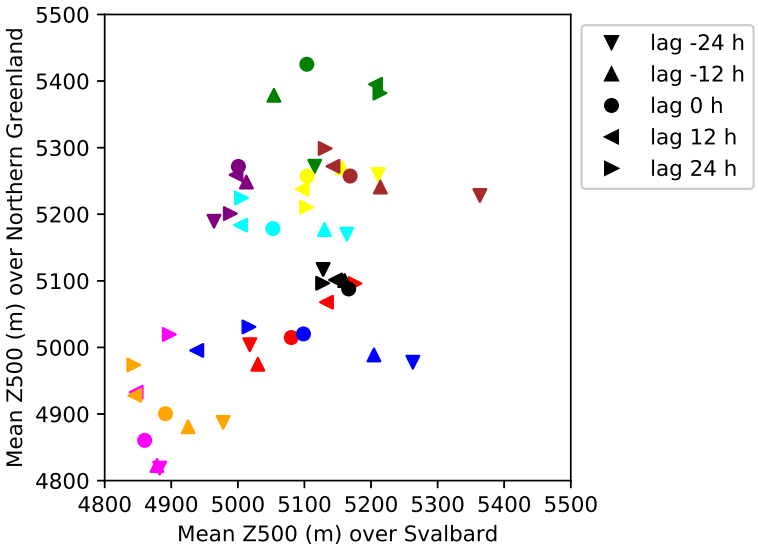

Figure 4.11: Same as Figure 4.6, but with lag 0 h as the time step with the largest peak.

low over Svalbard, it is higher over Greenland. Moist of the markers in Figure 4.11 are located in the upper left triangle of the figure, as expected. The event shown in magenta has a large increase in the mean Z500 over Northern Greenland and a small decrease over Svalbard. For the events shown in blue and cyan the decrease over Svalbard is larger than the increase over Northern Greenland. The event shown in orange has both a decrease over Svalbard and an increase over Northern Greenland. For the event shown in green the Z500 over Svalbard increases after the peak, which makes this event an exception from the probably most common situation.

4.3.2 Barents Sea

CAOs in the Barents Sea behave differently from those in the Fram Strait (Figure 4.12). There is an upper level cyclone sitting over Novaya Zemlya (Figure 4.12a). The MSLP patterns shows a weak cyclone over Northern Scandinavia. Figure 4.12a shows a northeastward tilt with height, but if the Z900 (contours in Figure 4.12b) and the Z900 (contours in Figure 4.12a) are compared, there is in fact a northwestward tilt with height. The Z500 contours (Figure 4.12a) show that there is a ridge over the eastern part of Greenland. According to the Z900 contours in Figure 4.12b, there is a trough west of Norway.

The sensible heat flux (Figure 4.12c) is large in the Fram Strait, north of Norway

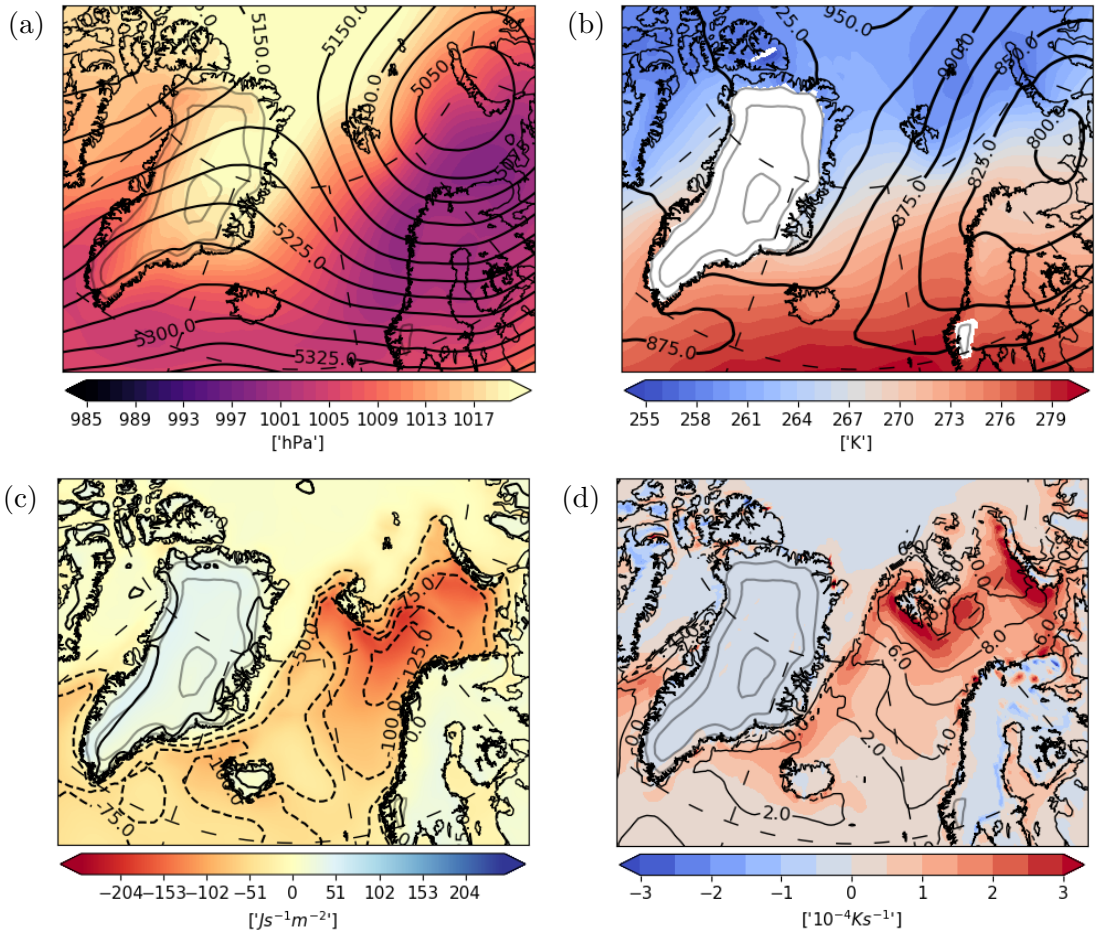

Figure 4.12: Same as Figure 4.9, but for CAOs in the Barents Sea associated with easterlies.

and west of Novaya Zemlya. North of Norway the latent heat flux is approximately 125 Wm^{-2}. The potential temperature tendency (Figure 4.12d) is large compared to the surroundings both west of Novaya Zemlya and west of Svalbard, approximately $3{\cdot}10^{-4}$ Ks^{-1}. This goes along with the Z900 contours (Figure 4.12b), which show a geostrophic wind from the east, hence advecting cold air masses from the sea ice and causing heat fluxes and diabatic heating.

4.3.3 Norwegian coast

In Figure 4.13a and Figure 4.13b, the synoptic conditions for CAOs outside the Norwegian coast are shown. The MSLP and Z500 pattern (Figure 4.13a) is similar to that of the Barents Sea, with an upper level cyclone sitting northeast of

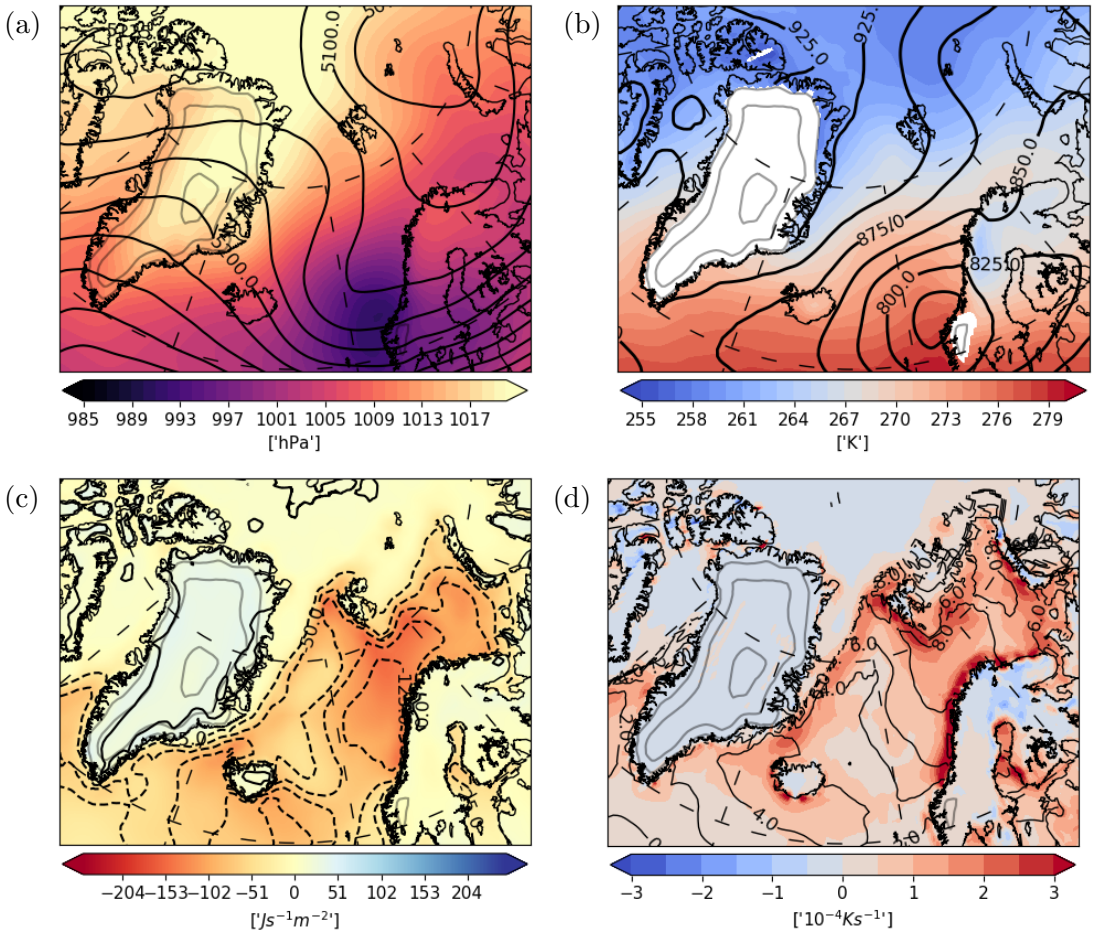

Figure 4.13: Same as Figure 4.9, but for CAOs outside the Norwegian coast associated with easterlies.

Novaya Zemlya. Also the potential temperature at 900 hPa and Z900 pattern (Figure 4.13b) is very similar. One difference is that there seems to be some cold air sitting over Northern Norway. The sensible heat fluxes (Figure 4.13c) are largest in the Fram Strait and there is also a region southeast of Svalbard with large values, approximately 150 Wm^{-2}. Figure 4.13d shows the potential temperature tendency together with the CAO index.

4.4 Composite standard deviations

This section presents the standard deviations of some of the composites. The composites give an indication on how a typical CAO looks like, but there might be

large variations. Thus, the standard deviations can tell how large the variations are. Only composites based on the maximum CAO index time steps are shown with standard deviations. The composite standard deviations are calculated as in Equation 2.16.

In Figure 4.14 and Figure 4.15, standard deviations of the MSLP and potential temperature at 900 hPa for CAOs in the Fram Strait are shown. The standard deviations of the MSLP (Figure 4.14a and Figure 4.15a) are large where the cyclones are located in the Barents Sea. This indicates that there are variations in the strength of the large scale cyclones that very likely give rise to CAOs in the Fram Strait. Also for the potential temperature at 900 hPa there are variations, up to 7 K (Figure 4.14b and Figure 4.15b). This goes along with the variations in the CAO index shown in Figure 4.1, which indicates variations in the intensity of CAOs.

Figure 4.16 shows the composites of the MSLP and potential temperature at 900 hPa with standard deviations. The standard deviation patterns are very similar to the previous ones, with variations in strength of the cyclone associated with CAOs (Figure 4.16a) and intensity of the CAOs (Figure 4.16b). Figure 4.16a indicate that there are standard deviations of 13–14 hPa over Scandinavia, where the cyclone is located.

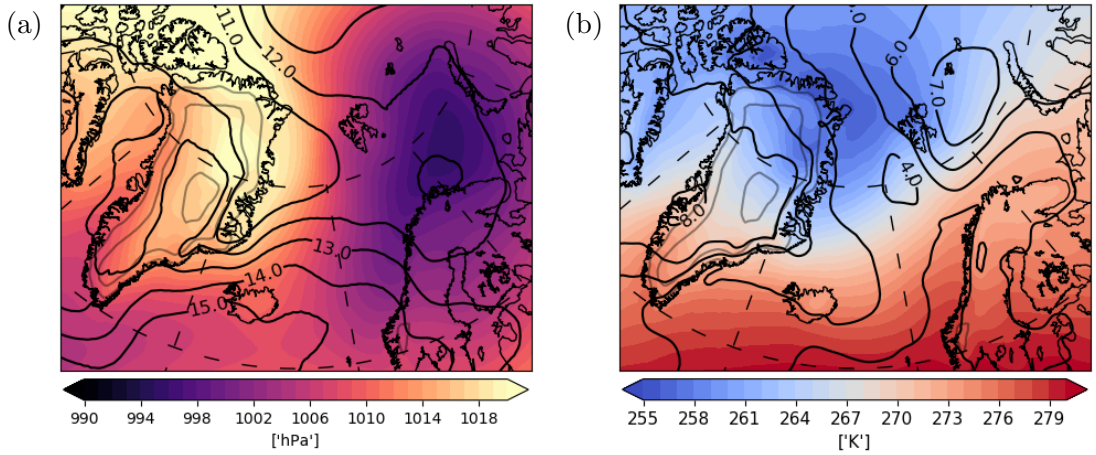

Figure 4.14: Composites of (a) MSLP and (b) potential temperature at 900 hPa with standard deviations as contours. The composites are based on the maximum CAO index during events in the Fram Strait associated with northerlies.

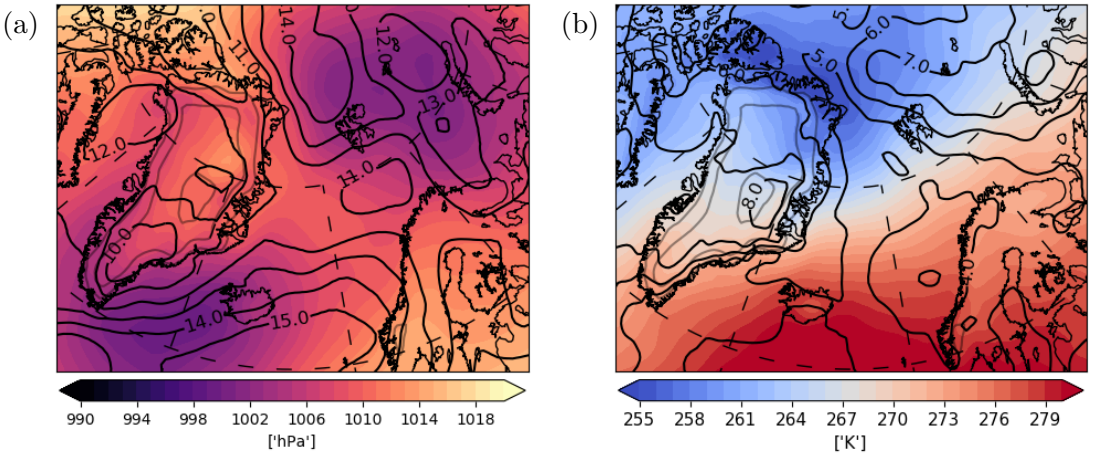

Figure 4.15: Same as Figure 4.14, but for events associated with westerlies.

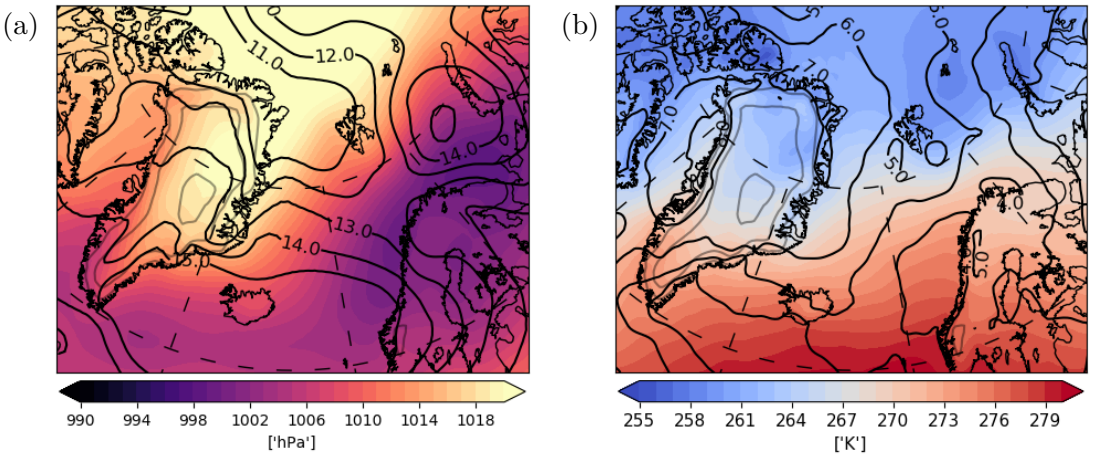

Figure 4.16: Same as Figure 4.14, but for CAOs in the Barents Sea associated with easterlies.

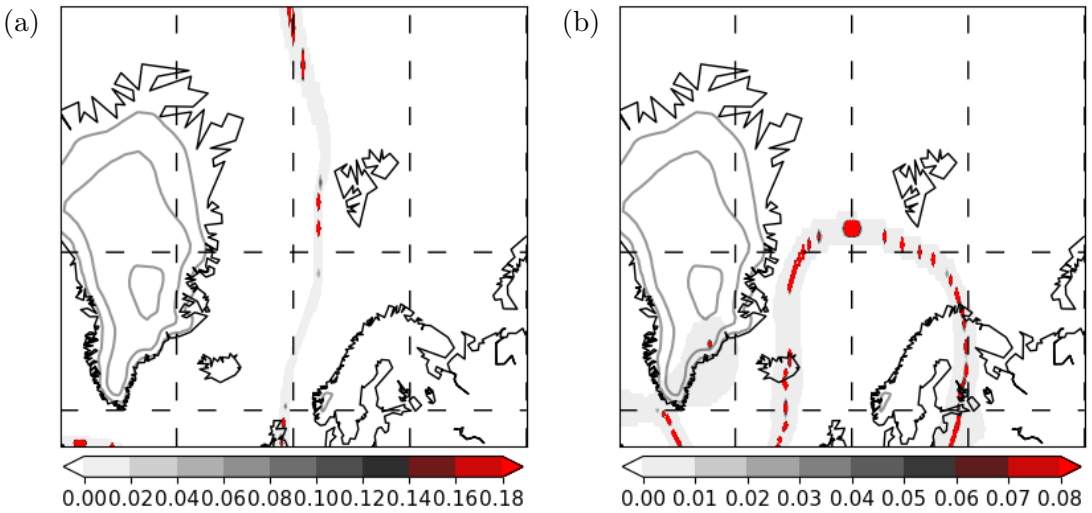

Figure 4.17: p-values in each grid point from the Wilcoxon test. The maps show the region in which the field significance test is performed. Note that the color scales are different in Figures (a) and (b).

4.5 Significance test

Composites of MSLP for events in the Fram Strait from the north at the maximum CAO index time steps are tested for significance. The test is performed as described in section 2.8. As mentioned in section 2.8, 10 000 artificial composites were calculated. The test was also done with only 1000 artificial composites (not shown), and the results were very similar.

Figure 4.17a shows p-values of the local tests for events in the Fram Strait associated with northerlies. In most grid points the p-values are close to 0, but in the middle of the map there are larger p-values. This indicates that the cyclone over the Barents Sea and the anticyclone over Greenland are characteristic for CAOs in the Fram Strait. The p-values for the events associated with westerlies are shown in Figure 4.17b. Here the p-values are close to 0 in most grid points, as in the case with northerlies (Figure 4.17a). However, the patterns are not completely similar. For the case with northerlies (Figure 4.17a), there is a line in the middle of the map from the north to the south where the p-values are larger than elsewhere. The other case (Figure 4.17b) shows that the p-values are large along a line from East Greenland and eastwards to south of Svalbard. The test was also done on MSLP anomalies with respect to climatology (not shown), with a similar result. In grid points where the anomalies were close to 0, the p-values were large, and elsewhere the p-values were approximately equal to 0.

The field significance test is performed as explained in section 2.8. For the case with northerlies (Figure 4.17a), 16 800 grid points are tested, and 16 775 local null hypotheses are rejected. The Bonferroni-type criterion described in Equation 2.17 gives a significance level $\alpha_{local} = 2.98 \cdot 10^{-6}$. The p-value of the global test (Equation 2.18) is $1.1 \cdot 10^{-16}$, which means that the global null hypothesis can be rejected on a 5 % significance level. For the case with westerlies (Figure 4.17b), 16 736 local null hypotheses are rejected. The Bonferroni-type criterion and the p-value of the global test is equal to that of the previous test. From this it can be concluded that the MSLP pattern is highly significant. However, there are some problems with significance testing. These problems are elaborated on in the paragraph below.

Several papers (for instance Nicholls (2001), Ambaum (2010)) have discussed disadvantages with significance tests. The main problem with a significance test is that it cannot tell how likely it is that the null hypothesis is true given the observation x, $P(H_0|x)$. What a significance test gives is the likelihood of getting a result at least as extreme as the observed result, given that the null hypothesis is true, $P(x|H_0)$ (the p-value of the test). These two probabilities are not the same. This misunderstanding is commonly dubbed "the error of the transposed conditional" (Ambaum, 2010). Masson (2011) suggests a Bayesian analysis as an alternative to hypothesis testing. The purpose of a Bayesian alternative is to estimate the probability that the null hypothesis is true given the observation, $P(H_0|x)$. Using Bayes theorem (Walpole et al., 2014) this probability is

$$P(H_0|x) = \frac{P(x|H_0)P(H_0)}{P(x)}. \tag{4.1}$$

This probability is not possible to find in this case, since one would need to know the *a priori* probability that H_0 is true, $P(H_0)$. Next, to estimate $P(H_0)$, one would need to do the composite analysis several times with different datasets. This is in general not possible in atmospheric science.

To summarize, the significance test performed does not provide a proof. However, the results are supported by physical reasoning.

Chapter 5

Frontogenesis along the CAO front

The introduction (chapter 1) raised the question if there could be frontal instabilities associated with CAOs. In this chapter frontogenesis along the CAO front is investigated. The different terms in the frontogenesis function (Equation 2.24) are calculated from ERA Interim. Frontal dynamics during CAOs are investigated through cross sections of potential temperatures, potential temperature tendencies and the different terms in the frontogenesis function. In addition, the magnitude of the horizontal potential temperature gradient, $|\nabla_H \theta|$ is investigated. The frontogenesis function is the total derivative of $|\nabla_H \theta|$. The cross sections are taken along the CAOs. The frontogenesis data are shown in intervals of 50 hPa from 950 to 800 hPa. First, the frontogenesis contributions for the case studies in chapter 3 are investigated. Next, composites of frontogenesis for CAOs in the Fram Strait and Barents Sea are discussed.

5.1 Case studies

This section investigates the change of the front during the CAOs chosen for the case studies in chapter 3. Cross sections are plotted along the CAOs close to the onset time steps.

5.1.1 Fram Strait

This section investigates the frontogenesis at the onset of the CAO studied in section 3.1. The wind at the onset of this CAO was predominantly from the north. The vertical cross sections in Figure 5.2 are plotted along the wind direction, with north and hence the ice edge is to the left, as shown in Figure 5.1a. In Figure 5.2b, the magnitude of the horizontal potential temperature gradient is plotted together with the total frontogenesis. The frontogenesis contours can be interpreted as streamlines, which means that they describe the frontal circulation according to the Sawyer–Eliassen equation (subsection 2.9.2, Equation 2.29). The circulation is thermally direct and anticlockwise at 200–300 km from the ice edge. The eccentricity of the circulation indicates that vertical motions are suppressed near the ice edge. From Figure 5.2b it is also clear that the circulation is around the front. Looking at the magnitude of the horizontal potential temperature gradient throughout the CAO (not shown) the front is moving southwards and the frontogenesis becomes less intense after the peak time step.

The potential temperature contours in Figure 5.2a indicate a well defined front close to the ice edge, which goes along with the magnitude of the horizontal potential temperature gradient at 0–200 km (Figure 5.2b). From the contours in Figure 5.2a it can also be seen that the mixing layer (the layer where the potential temperature gradient is small, Stull (2012)) is shallow near the ice edge and it increases with the distance from the ice edge. This goes along with the sketch in figure 1 in Renfrew and King (2000). The paper by Renfrew and King (2000) presents a model of the convective internal boundary layer. The model is tested on two CAOs. The mixing layer structure is also consistent with Hartmann et al. (1997) which is a study of the boundary layer during a CAO in the Fram Strait in October 1991.

Looking at differential heating and tilting together (Figure 5.2c), it is clear that the heating and tilting terms work against each other close to the ice edge. The change in the heating gradient is largest close to the ice edge. The tilting term tries to make the front weaker, but the heating term has a stronger positive contribution so the total frontogenesis is positive as shown in Figure 5.2b. 200 km away from the ice edge the differential heating is negative, and hence frontolytic ($\approx -20 \cdot 10^{-10}$ $\mathrm{Km^{-1}s^{-1}}$). The tilting term is positive and hence frontogenetic at this location, approximately 5–10 $\cdot 10^{-10}$ $\mathrm{Km^{-1}s^{-1}}$.

Figure 5.2d shows frontogenesis by divergence and deformation together. 300 km away from the ice edge the deformation term is largest. The divergence term is frontogenetic south of the ice edge and it becomes frontolytic 400 km away from the ice edge.

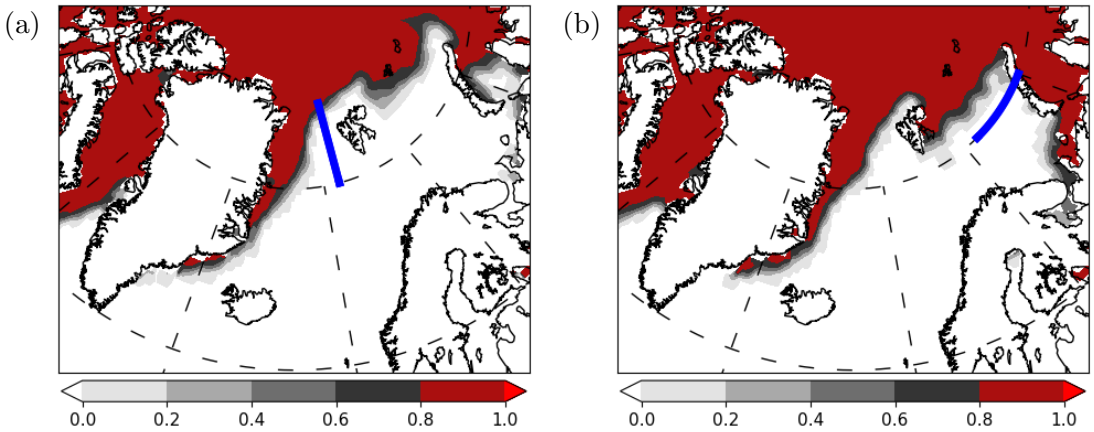

Figure 5.1: Sea ice cover (fraction of grid point covered by sea ice) on (a) December, 25, 18:00 and (b) January 17, 18:00. The blue lines indicates where the cross sections are taken for the case studies.

5.1.2 Barents Sea

The CAO in the Barents sea investigated in chapter 3 had easterlies at the onset. Hence, the cross sections are plotted with west to the left and east to the right as shown in Figure 5.1b. The frontogenesis contributions for the event in the Barents Sea are shown in Figure 5.3. The time step shown is January 14, 18:00, which is three days after the onset. Figure 5.3b indicates that there is a front at approximately 600–650 km, west of Novaya Zemlya. Right east of the front there is frontogenesis. There is also frontogenesis further west in the cross section, but not as much as in the east. After this time step the frontogenesis becomes less intense, but when the CAO becomes more intense with respect to the CAO index in the region (the peaks in the time series shown in Figure 3.6 are approached), the circulation is also intensified (not shown). The streamlines indicate that horizontal motions are suppressed. This is the case throughout the entire CAO (not shown). The mixing layer close to Novaya Zemlya is shallower in this case than in the previous case study. As for the previous case study, the depth of the mixing layer is increasing with distance from the ice edge.

The differential heating term is frontogenetic near Novaya Zemlya (to the right in Figure 5.3c). Also the tilting term is frontogenetic. In the very eastern part of the cross section, where there is frontolysis according to Figure 5.3b, the tilting term is frontolytic. The deformation term is frontolytic at the lower part of the section (Figure 5.3d), and the divergence term is frontogenetic. These two terms contribute less to frontogenesis than the tilting and the differential heating. From Figure 5.3c and Figure 5.3d it seems like the tilting term is the largest contributor

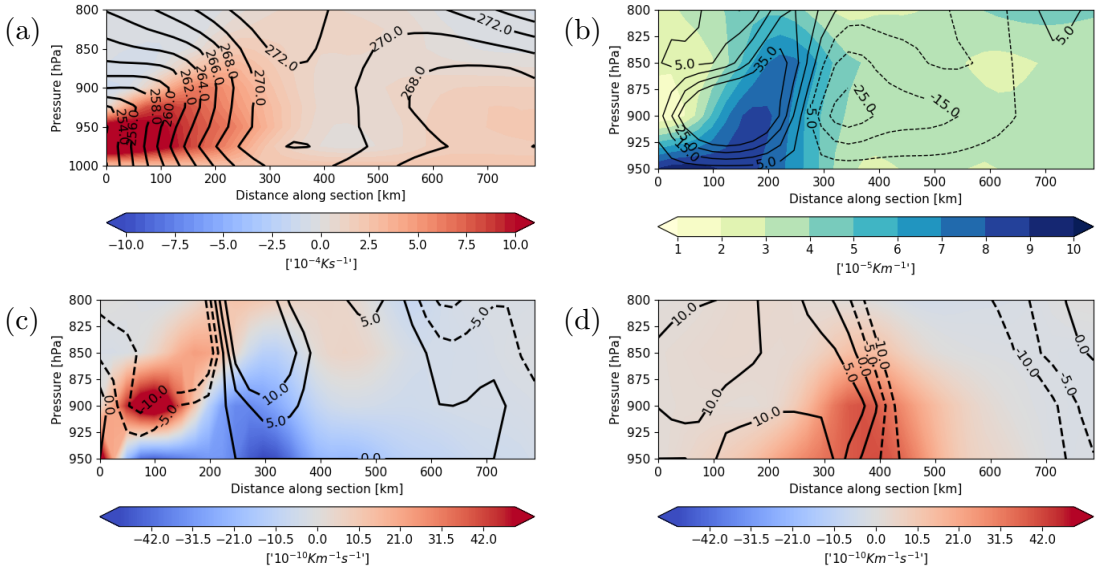

Figure 5.2: Cross sections of diabatic heating, frontogenesis and the different contributions to frontogenesis at December 24, 2015, 18:00. The sections are taken as shown in Figure 5.1a. The variables shown are (a) potential temperature tendency (10^{-4} Ks^{-1}; shading) and potential temperature (K; contours), (b) magnitude of the horizontal potential temperature gradient (10^{-6} Km^{-1}; shading) and total frontogenesis (10^{-10} Km$^{-1}s^{-1}$; contours), (c) frontogenesis by differential heating (10^{-10} Km$^{-1}s^{-1}$; shading) and tilting (10^{-10} Km$^{-1}s^{-1}$; contours) and (d) frontogenesis by deformation (10^{-10} Km$^{-1}s^{-1}$; shading) and divergence (10^{-10} Km$^{-1}s^{-1}$; contours).

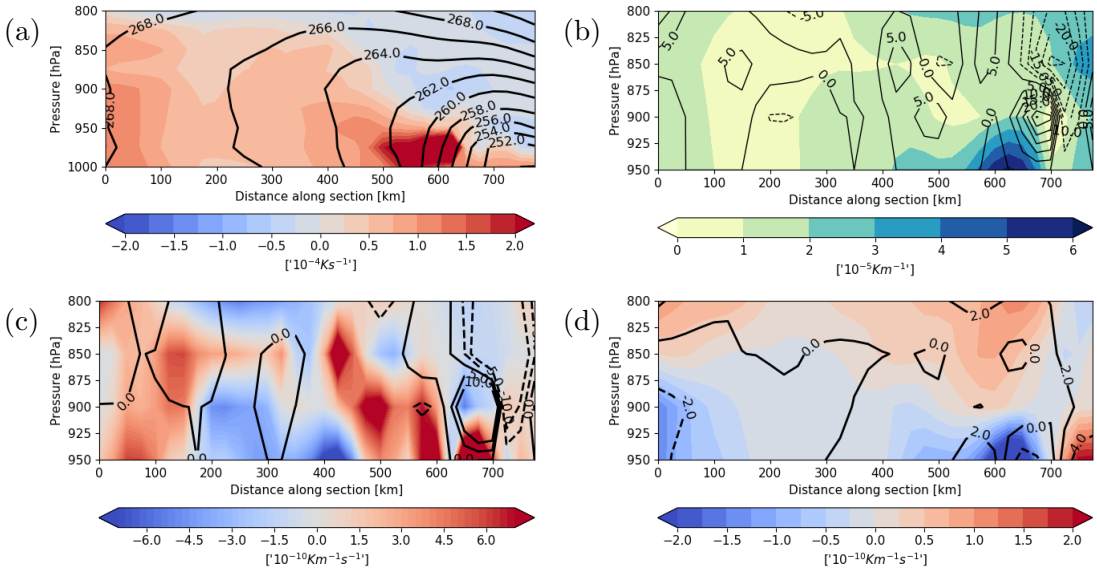

Figure 5.3: Same as Figure 5.2, but for the case study of the event in the Barents Sea. The sections are taken as shown in Figure 5.1b, and the time step is January 14, 2015, 18:00.

to the frontogenesis close to Novaya Zemlya.

5.2 Composites of frontogenesis

5.2.1 CAOs in the Fram Strait associated with northerlies

The front in the composite cross section of diabatic heating and potential temperature (Figure 5.5a) is not as well defined as that for the case study (Figure 5.2a). This may be due to different locations of the ice edge and hence the front for the 250 events included in the composite (Table 4.1). In general composites are smoother than single cases. Figure 5.5 shows composite cross sections of the different contributions to frontogenesis. The sections are taken as shown in Figure 5.4a, i.e., along the CAO. In Figure 5.5b, the magnitude of the horizontal potential temperature gradient is plotted together with the total frontogenesis. The magnitude is largest at 950–925 hPa and at 100–200 km from the ice edge. The frontogenesis contours in Figure 5.5b give an indication of the streamlines of the frontal circulation described by the Sawyer–Eliassen equation. The circulation is thermally direct (cold air is sinking and warm air is rising) and anticlockwise, with cold air to the left. According to the eccentricity of the circulation, vertical motion is sup-

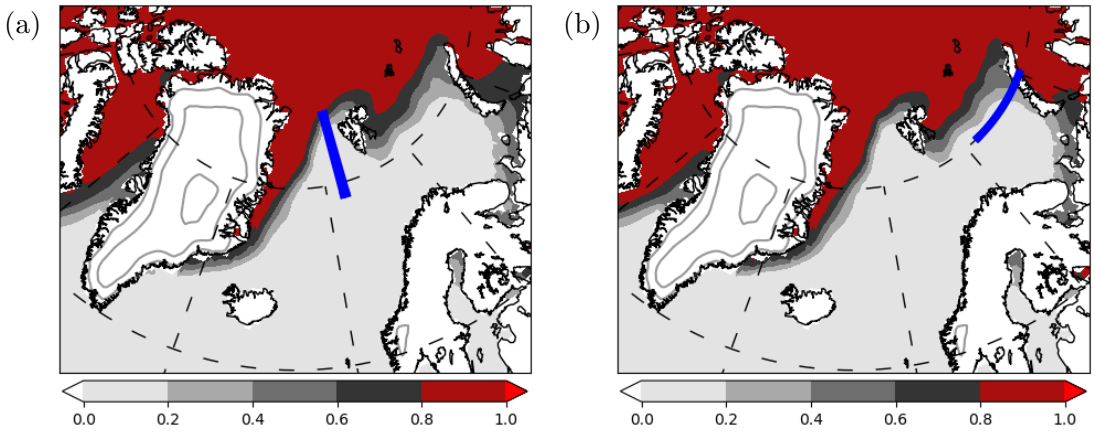

Figure 5.4: Composites of sea ice cover for (a) CAOs in the Fram Strait associated with northerlies and (b) CAOs in the Barents Sea associated with easterlies. The composites are based on the onset time steps. The blue lines show where the cross sections are taken.

pressed. This resembles the streamlines from the case study in subsection 5.1.1 The circulation is slightly shifted towards the south of the front (Figure 5.5b). This indicates that the front is moving towards the south as the intensification of the front is located south of the front. The circulation during CAOs in the Barents Sea associated with northerlies is similar (not shown). The potential temperature contours in Figure 5.5a show a mixing layer with increasing depth as for the case study in subsection 5.1.1, but the increase is less for the composite.

Figure 5.5c shows vertical composite cross sections of the differential heating together with tilting. The differential heating is positive near the ice edge, which means that it is a frontogenetic term. There is a strong gradient in diabatic heating, which also can be seen from Figure 5.5a. The tilting term is negative, and hence frontolytic. During the time lags it becomes more negative (not shown), implying that the isentropes would become more horizontal if this was the only contribution to frontogenesis. However, the differential heating term is strongly positive near the ice edge, contributing to maintenance of the front. In Figure 5.5d, the deformation and divergence terms are shown together. Between 950 and 920 hPa the deformation term is positive (frontogenetic). The divergence term is frontogenetic everywhere. This means that there is frontogenesis due to convergence of isentropes. The deformation term is frontogenetic in the lowest part of the map and it is close to 0 further aloft.

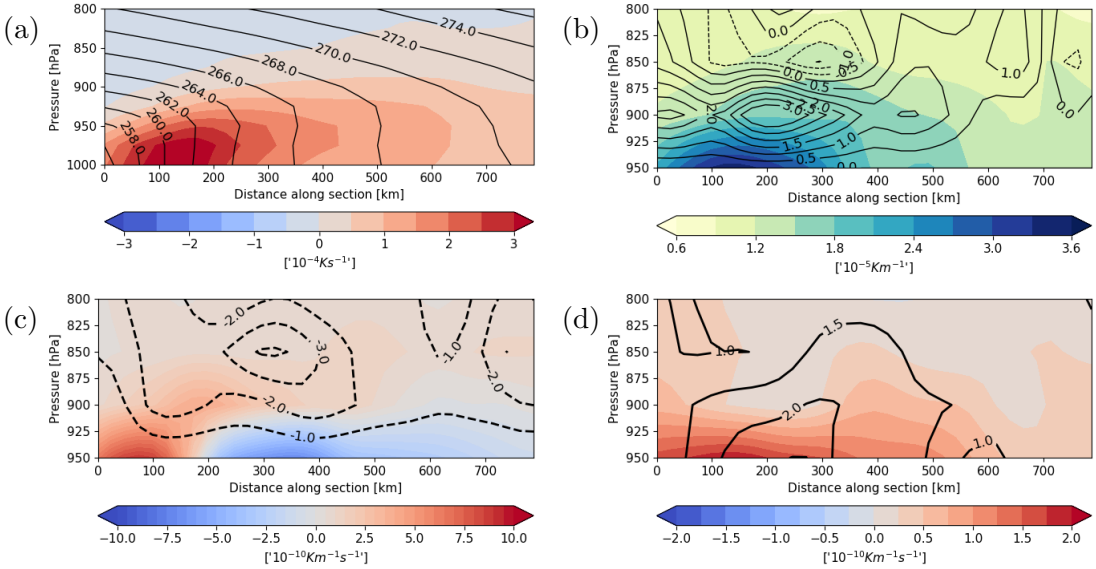

Figure 5.5: Composite cross sections of the different contributions to frontogenesis based on the onset time steps for CAOs in Fram Strait associated with northerlies. The cross sections are taken as shown in Figure 5.4a. The subfigures are as in Figure 5.2.

5.2.2 CAOs in the Barents Sea associated with easterlies

The frontogenesis contributions at the onset of CAOs in the Barents Sea associated with easterlies are shown in Figure 5.6, with the cross sections taken as shown in Figure 5.4b. Figure 5.6b shows the magnitude of the horizontal potential temperature gradient together with the frontogenesis. West of Novaya Zemlya there is a front. The frontogenesis contours show that there is frontogenesis east of the front and frontolysis in the west. Hence, the circulation east of the front is anticlockwise, whereas on the western side the circulation is clockwise. Further west, at approximately 400 km there is also a potential temperature gradient. From the frontogenesis contours at this location it can be seen that the gradient is intensified.

The different terms in the frontogenesis function are shown in Figure 5.6c and Figure 5.6d. At approximately 650 km in Figure 5.6c the differential heating term is more frontogenetic than elsewhere. According to Figure 5.6a there is a gradient in the potential temperature tendency. This gradient is intensified, hence contributing to frontogenesis. The tilting term (contours in Figure 5.6c) is frontogenetic near Novaya Zemlya and frontolytic further west. In Figure 5.6d the deformation and divergence terms are shown. The deformation in shading is

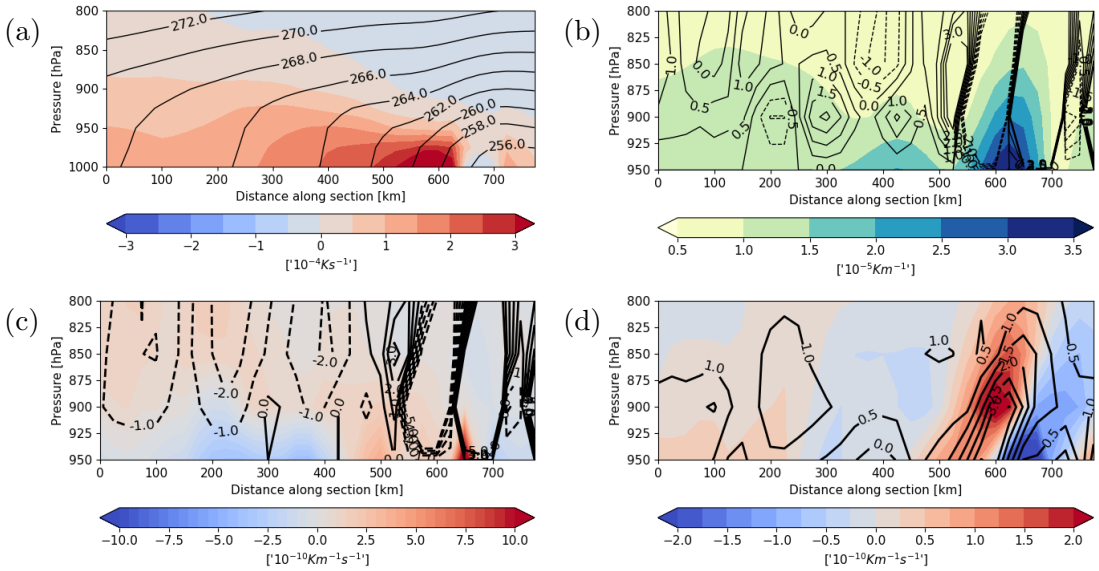

Figure 5.6: Same as Figure 5.5, but for events in the Barents Sea associated with easterlies. The cross sections are taken as shown in Figure 5.4b, with east to the right.

frontolytic near Novaya Zemlya and frontogenetic further west, at 500–600 km in the cross section. The divergence term is frontogenetic where the front is located (contours in Figure 5.6d).

Chapter 6

Caveats and shortcomings

This chapter provides a critical look on the work presented in this thesis, with some suggestions for improvements. The most important shortcomings are the procedure for detecting CAOs, the choice of regions, and the method for separating the CAOs with respect to the wind direction at the peak time steps (for details see section 2.6).

In the procedure for determining the threshold for the CAO index, the 50th percentile of the local maxima in the running mean time series was calculated (for details see section 2.5). When the time period between two local maxima was less than 10 time steps, only the largest local maximum was included in the list of local maxima used for calculating the threshold for the CAO index. This threshold was used to determine when a CAO starts and ends. This procedure gave some CAOs with a duration of one month or longer, as shown in section 4.1. Time series of some of the long-lived CAOs have been shown in Figure 4.3 and Figure 4.4. From these time series it was evident that the CAOs with the longest duration consisted of several pulses of cold air. The running mean, however, prevented the index to drop below the threshold, which means that these CAOs should probably be treated as several separate CAOs. In the following paragraphs possible solutions to this problems are discussed.

The algorithm could be expanded by requiring that if the difference between a local maximum and the neighboring local minimum is larger than a certain threshold, the event should be split into two events. Another possibility is to increase the threshold for the CAO index, for instance by requiring that the time period between two local maxima in the running mean has to be larger than 10 time steps (as used in this work, see section 2.5) in order to include both maxima in the threshold calculation. Nevertheless, if the CAO index threshold is too high, less

intense events will be missed.

If the long-lived events were split into separate CAOs, the composites would most likely look very similar. The only difference is that the composite would contain more members, which means that the long-lived CAOs are not likely to be problematic for the analysis presented in this thesis.

The regions investigated could have been chosen differently. For instance, the East Greenland box was probably not necessary, as several events occurring there occurred simultaneously with events in the Fram Strait box, implying the same events were detected in both boxes. The Norwegian coast box could have been shrunk in the south. In this way, it is likely that more CAOs would be detected in this box, because less grid points in the south with low values of the CAO index are included in the mean CAO index in the box.

The procedure for separating CAOs with respect to the wind direction at the peak time steps does not necessarily indicate where the cold air masses are coming from. The reason for this is that the wind direction at the onset and at the peak of a CAO is not necessarily the same. For instance, in the Fram Strait, the composite of events associated with westerlies indicates that the geostrophic wind at 900 hPa is predominantly from the north, and it turns towards westerlies. The composites based on events in the Barents Sea associated with easterlies showed that the wind direction at the onset was predominantly from the east. To determine where the cold air is actually coming from, a trajectory analysis similar to the one Papritz and Spengler (2017) is required.

Chapter 7

Summary and conclusions

In chapter 1, the following questions were raised:

1. Is there a typical synoptic situation associated with CAOs?
2. How are the frontal dynamics during CAOs?
3. Do CAOs have different properties in the different regions?

To answer these questions, CAOs in the Norwegian and Barents Sea have been investigated, with focus on the synoptic conditions, heat fluxes, potential temperature tendencies and frontal dynamics. Four regions have been chosen as shown in Figure 1.1, where the main focus has been on the Fram Strait and the Barents Sea box. A CAO index has been defined, and an algorithm for detecting CAOs using the CAO index and time series analysis (section 2.5) has been developed. Composites based on the peaks in the time series defining CAOs and composites based on the onset time steps for the CAOs have been calculated (chapter 4). To supplement the composites, two case studies have been performed (chapter 3).

7.1 Synoptic conditions

The case and composite studies indicate that there is a typical synoptic situation associated with CAOs. It is common that a mid-latitude cyclone is progressing northwards and when the cyclone is located at approximately 70–75 degrees north, it is advecting cold air from the ice edge. This goes along with the fact that polar lows often occur after severe weather in Northern Norway due to mid-latitude cyclones (Noer, 2018).

The composites based on CAOs associated with northerlies indicate that it is common that the MSLP and the geopotential heights are low in the Barents Sea and high over Greenland (Figure 4.14). Cyclones sitting in the Barents Sea produce northerlies through the Fram Strait, hence cold air is advected southwards off the ice edge.

For CAOs associated with westerlies, the pattern is slightly different (Figure 4.15). In these composites the cyclones in the Barents Sea are located further north and the cyclones are weaker than for the previous composites. Over Greenland the MSLP is lower than during CAOs associated with northerlies. This means that the difference in MSLP between Greenland and the Barents Sea is less for CAOs associated with westerlies than for those associated with northerlies. From this it can be concluded that CAOs in the Fram Strait associated with northerlies are also associated with the strongest geostrophic winds close to the surface.

Both the composites based on CAOs associated with northerlies and westerlies show standard deviations around 12–14 hPa where the cyclones are located, which means that the strength of the cyclones is varying. CAOs in the box outside the Norwegian coast are most often advection of cold air masses from the north. These cold air masses are coming from the Fram Strait or from the Barents Sea. Advection of cold air masses from the Norwegian mainland is less common.

Composites of MSLP based on CAOs in the Fram Strait associated with northerlies and westerlies have been tested for significance using a field test (section 4.5). The p-values of the tests indicate that the MSLP pattern is highly significant for both types of CAOs in the Fram Strait.

7.2 Heat fluxes

Cold air moving over relatively warmer sea gives rise to large heat fluxes. The heat fluxes for the case and composite studies indicate that during CAOs, the sensible heat flux is large compared to the surroundings in the area over the sea where the cold air is advected. In general the sensible heat flux is larger than the latent heat flux. This goes along with Papritz and Spengler (2017) who found that for CAOs forming over cold water close to the ice edge extracts sensible heat more efficiently than latent heat. The latent heat flux is limited by the saturation specific humidity with respect to SST (Papritz et al., 2015).

Comparing CAOs in the Fram Strait and Barents Sea, it can be concluded that CAOs in the Fram Strait are associated with the largest heat fluxes. This indicates that the Fram Strait has more intense CAOs than the Barents Sea. During CAOs

outside the Norwegian coast, the heat fluxes are weaker than during CAOs in the Fram Strait and Barents Sea. This goes along with the conclusion that CAOs outside the Norwegian coast are less intense. One reason for this might be that when cold air masses from the ice in the north are advected into the sea outside Norway, these air masses are already heated by the strong sensible heat fluxes. Hence, the CAO index is in general lower at latitudes south of Svalbard.

7.3 Frontogenesis

The total frontogenesis and the different terms in the frontogenesis function have been investigated for both composites and case studies (chapter 5). Also the relation between the potential temperature and the potential temperature tendency has been investigated. Comparing the cross sections of the potential temperature and the total frontogenesis, the front is more pronounced in the case studies than in the composites. The circulation can be inferred from the total frontogenesis.

In the case study by Grønas and Skeie (1999), a similar result is presented, with a thermally direct circulation at the Arctic front. The eccentricity of the circulation varies between the Fram Strait and Barents Sea (chapter 5). For CAOs in the Fram Strait associated with northerlies, the circulation tend to be such that vertical motions are suppressed, whereas for CAOs in the Barents Sea associated with easterlies, it is the other way around. The cross sections of the potential temperature and the potential temperature tendency show that the mixing layer during CAOs is shallow near the ice edge, and the depth increases further away from the ice edge. The depth of the mixing layer varies between the case and composite studies. For the case study of the CAO in the Fram Strait the depth of the mixing layer is approximately 75 hPa at 0 km (Figure 5.2a). At approximately 200 km the depth has doubled. The composite of the mixing layer for CAOs associated with northerlies shows a shallower mixing layer than the case study (Figure 5.5a). Here the depth starts at 50 hPa, and it does not increase much with the distance from the ice edge, unlike the case study. The case study of the CAO in the Barents Sea shows a shallow mixing layer at the western coast of Novaya Zemlya (Figure 5.3a). The depth a this location is 30–40 hPa, and it increases to approximately 100 hPa 480–500 km. For the composites of CAO in the Barents Sea associated with easterlies the mixing layer is approximately 25 hPa west of Novaya Zemlya (Figure 5.6a). This mixing layer is not increasing much with distance from Novaya Zemlya. At around 400 km the depth is 50–75 hPa.

7.4 Concluding remarks

To summarize, the main conclusions are:

1. Is there a typical synoptic situation associated with CAOs?

    - CAOs are often associated with large scale cyclones. The cyclones advect the cold air from the ice edge. The wind direction at the largest peak in the running mean defining the CAOs inside the box where a CAO is detected is most often predominantly from the north. However, there are CAOs where the wind direction is from the east or from the west at the time step with the largest peak within the event.

    - During CAOs in the Fram Strait there is a surface cyclone sitting in the Barents Sea, advecting cold air from the north. When there are CAOs in the Barents Sea the cyclone is located further east.

    - The CAOs in the Barents Sea investigated in this work are associated with easterlies. During these CAOs the composites showed that there is typically a surface cyclone sitting over Northern Scandinavia.

    - During CAOs in the Fram Strait the Z500 is increasing over Greenland and decreasing over Svalbard for some of the most intense CAOs in this region.

    - During CAOs outside the Norwegian coast associated with easterlies there is a cyclone sitting west of southern Norway, advecting cold air from the east. The cold air may come from the sea ice in the Northern Barents Sea or from the Norwegian mainland.

2. How are the frontal dynamics during CAOs?

    - Before the onset of a CAO there is a front at the ice edge separating cold air over the ice from warmer air over the sea. At the onset the front is moving off the ice edge.

    - The eccentricity of the residual circulation is different during CAOs in the Fram Strait and in the Barents Sea. The composites based on CAOs in the Fram Strait associated with northerlies show that the eccentricity of the circulation is such that vertical motions are suppressed relative to horizontal motions. During CAOs in the Barents Sea associated with northerlies the circulation is similar, but the streamlines are less tight (not shown). For CAOs in the Barents Sea associated with easterlies the eccentricity of the circulation is such that horizontal motions are suppressed.

- During CAOs in the Fram Strait associated with northerlies the tilting term in the frontogenesis function is frontolytic, whereas the other terms are frontogenetic close to the ice edge. The same applies for CAOs in the Barents Sea associated with easterlies.
- For the case study of the CAO in the Fram Strait the circulation was closely following the front. This was not the case for the other results. For the case study of the CAO in the Barents Sea the frontogeneis was located slightly east of the front (Figure 5.3b). The composite cross section based on CAOs in the Fram Strait associated with northerlies (Figure 5.5b) show that the frontogenesis is located slightly south of the front, indicating that the front is moving southwards. The composite cross section based on CAOs in the Barents Sea associated with easterlies (Figure 5.6b) show that there is frontogenesis slightly east of the front and frontolysis slightly west of the front.

3. Do CAOs have different properties in the different regions?
   - CAOs are in general most intense in the Fram Strait. Also in the Barents Sea there are intense events, but not as many as in the Fram Strait.
   - The Fram Strait is the region where most CAOs occur, and least CAOs occur outside the Norwegian coast.
   - The least intense CAOs occur in the East Greenland and Norwegian coast boxes. This is expected because these boxes are located further south.
   - CAOs in the Norwegian coast box are normally advection of cold air from the north. This also applies for CAOs in East Greenland.

Chapter 8

Outlook

This chapter presents some natural extensions of this work. Possible interesting research topics are the predictability of CAOs and how CAOs might change in the future. Also the frontogenesis and frontolysis during CAOs can be further investigated.

8.1 Frontogenesis and the Sawyer–Eliassen equation

The frontogenesis could be further investigated by solving the Sawyer–Eliassen equation (for details see subsection 2.9.2) numerically or analytically. From the solution of the Sawyer–Eliassen equation the stream function can be plotted together with the potential temperature gradient. The shape of the stream function would show the relative importance of the different terms in the Sawyer–Eliassen equation. Furthermore, it can be hypothesized that the circulation might contribute to accelerate the CAO flow, which could be seen as a positive feedback to the CAO.

8.2 Other reanalysis datasets

The method for detecting CAOs can be used on other datasets. One alternative dataset that could be used is ERA-5 (Hersbach and Dee, 2016). ERA-5 is the newest reanalysis dataset from ECMWF, and it will eventually replace ERA Interim (Hersbach and Dee, 2016). When the full ERA-5 dataset is available in

early 2019, it will have a higher resolution than ERA Interim, both in time and in space. The analysis fields will be available at a horizontal resolution of 31 km on 137 vertical levels, with a time increment of 1 hour. Furthermore, uncertainty measurements will be available from a 10-member ensemble of data assimilation. The time increment of the ensemble is 3 hours.

Another dataset that can be used for research on CAOs is the Arctic System Reanalysis (ASR) (Bromwich et al., 2001, 2010, 2016). ASR is a high resolution reanalysis dataset with a domain covering the mid- and high latitudes of the Northern Hemisphere (Bromwich et al., 2016). The dataset has both a low and a high resolution system and an inner and outer domain, according to figure 1 in Bromwich et al. (2016). The inner domain has a high resolution system with a resolution of 15 km. The resolution in time is 1.5 hours. With a finer resolution mesoscale phenomena would be better resolved. CAOs and polar lows are mesoscale phenomena, hence it is advantageous to use a data set with finer resolution for investigating these events.

8.3 Predictability of CAOs

The predictability of CAOs could also be an extension of this thesis. As mentioned in chapter 1, CAOs can lead to severe weather. Hence, good forecasts of these events are important. ECMWF operational and seasonal forecasts could be compared to ERA-5 or ASR. Comparing the forecast to a reanalysis dataset would give an indication of how well CAOs are forecasted. The quality of the forecast could be evaluated using the verification methods described in chapter 9 in the book of Warner (2010). For instance, the accuracy of the forecast could be evaluated by investigating how well the CAO index was forecasted. This could be measured by calculating the mean squared error and the bias. Warner (2010) also presents measures that could be applied to evaluate the ability to forecast CAOs. A contingency table (forecast matrix in terms of hits and misses) could be made to investigate whether CAOs were forecasted correctly. Furthermore, the forecast could be compared to a climatological average by calculating different skill scores such as Heidke skill score and Gilbert skill score (Warner, 2010). One could also perform a feature based forecast evaluation with respect to CAOs. Feature based means to detect CAOs and assess their occurrence, strength, variability and other properties instead of just doing statistics on certain variables. One could detect other phenomena in addition associated with CAOs such as large scale cyclones and fronts and assess the properties of these phenomena. The purpose of a feature based evaluation would be to assess how well the properties of CAOs are

forecasted.

8.4 CAOs in the future

The change of CAOs in the future is another possibility for further research. As outlined in chapter 1, CAOs play a significant role for weather and climate at higher latitudes. It is well known that the climate is changing, hence it is worthwhile to investigate how CAOs will respond to climate change.

Kolstad and Bracegirdle (2008) found that CAOs in the future likely will become less intense because the ice edge will move further north. This reduction in intensity comes from the fact that the difference between the sea and the cold air masses will decrease. Less sea ice results in more open water. They also found that polar lows will have a longer life time over open water before they hit land, which might contribute to an increased intensity of polar lows. With this in mind, it could be interesting to do further research on CAOs in the future. To do this a climate model well suited to study future CAOs should be selected, for instance a climate model from the Coupled Model Intercomparison Project (CMIP) (Taylor et al., 2012; Eyring et al., 2016). The purpose of CMIP is to improve knowledge about climate change. Following the methods presented in chapter 2, the CAO index can be calculated. Next, the procedure for detecting CAOs can be used on the climate model. When the CAOs has been detected composites can be calculated to investigate further how CAOs might look in the future.

To summarize, both operational forecast and future change of CAOs are highly relevant research topics since CAOs affect the weather and climate by contributing to the Atlantic meridional overturning circulation and giving rise to polar lows, which was outlined in chapter 1.

Bibliography

Ambaum, M. H., 2010: Significance tests in climate science. *Journal of Climate*, **23 (22)**, 5927–5932.

Benjamini, Y. and Y. Hochberg, 1995: Controlling the false discovery rate: a practical and powerful approach to multiple testing. *Journal of the royal statistical society. Series B (Methodological)*, 289–300.

Benjamini, Y. and D. Yekutieli, 2001: The control of the false discovery rate in multiple testing under dependency. *Annals of statistics*, 1165–1188.

Bracegirdle, T. J. and E. W. Kolstad, 2010: Climatology and variability of southern hemisphere marine cold-air outbreaks. *Tellus A*, **62 (2)**, 202–208.

Bromwich, D., Y.-H. Kuo, M. Serreze, J. Walsh, L.-S. Bai, M. Barlage, K. Hines, and A. Slater, 2010: Arctic system reanalysis: call for community involvement. *Eos, Transactions American Geophysical Union*, **91 (2)**, 13–14.

Bromwich, D. H., K. M. Hines, and L.-S. Bai, 2001: Arctic system reanalysis.

Bromwich, D. H., A. B. Wilson, L.-S. Bai, G. W. Moore, and P. Bauer, 2016: A comparison of the regional arctic system reanalysis and the global era-interim reanalysis for the arctic. *Quarterly Journal of the Royal Meteorological Society*, **142 (695)**, 644–658.

Businger, S., 1985: The synoptic climatology of polar low outbreaks. *Tellus A: Dynamic Meteorology and Oceanography*, **37 (5)**, 419–432.

Carleton, A. M. and Y. Song, 1997: Synoptic climatology, and intrahemispheric associations, of cold air mesocyclones in the australasian sector. *Journal of Geophysical Research: Atmospheres*, **102 (D12)**, 13 873–13 887.

Cushman-Roisin, B. and J.-M. Beckers, 2011: *Introduction to geophysical fluid dynamics: physical and numerical aspects*, Vol. 101. Academic Press.

Dee, D., et al., 2011: The era-interim reanalysis: Configuration and performance of the data assimilation system. *Quarterly Journal of the royal meteorological society*, **137 (656)**, 553–597.

Eady, E. T., 1949: Long waves and cyclone waves. *Tellus*, **1 (3)**, 33–52.

Eliassen, A., 1962: On the vertical circulation in frontal zones. *Geofys. publ*, **24 (4)**, 147–160.

Eyring, V., S. Bony, G. A. Meehl, C. A. Senior, B. Stevens, R. J. Stouffer, and K. E. Taylor, 2016: Overview of the coupled model intercomparison project phase 6 (cmip6) experimental design and organization. *Geoscientific Model Development*, **9 (5)**, 1937–1958.

Fletcher, J., S. Mason, and C. Jakob, 2016: The climatology, meteorology, and boundary layer structure of marine cold air outbreaks in both hemispheres. *Journal of Climate*, **29 (6)**, 1999–2014.

Grønas, S. and P. Skeie, 1999: A case study of strong winds at an arctic front. *Tellus A*, **51 (5)**, 865–879.

Hartmann, J., C. Kottmeier, and S. Raasch, 1997: Roll vortices and boundary-layer development during a cold air outbreak. *Boundary-Layer Meteorology*, **84 (1)**, 45–65.

Hersbach, H. and D. Dee, 2016: Era5 reanalysis is in production. *ECMWF Newsletter*, **147 (7)**.

Kolstad, E. W., 2011: A global climatology of favourable conditions for polar lows. *Quarterly Journal of the Royal Meteorological Society*, **137 (660)**, 1749–1761.

Kolstad, E. W. and T. J. Bracegirdle, 2008: Marine cold-air outbreaks in the future: an assessment of ipcc ar4 model results for the northern hemisphere. *Climate Dynamics*, **30 (7-8)**, 871–885.

Kolstad, E. W., T. J. Bracegirdle, and I. A. Seierstad, 2009: Marine cold-air outbreaks in the north atlantic: temporal distribution and associations with large-scale atmospheric circulation. *Climate dynamics*, **33 (2-3)**, 187–197.

Lin, Y.-L., 2007: *Mesoscale dynamics*. Cambridge University Press.

Mansfield, D., 1974: Polar lows: The development of baroclinic disturbances in cold air outbreaks. *Quarterly Journal of the Royal Meteorological Society*, **100 (426)**, 541–554.

Markowski, P. and Y. Richardson, 2011: *Mesoscale meteorology in midlatitudes*, Vol. 2. John Wiley & Sons, 4 pp.

Marshall, J. and R. A. Plumb, 2016: *Atmosphere, ocean and climate dynamics: an introductory text*, Vol. 21. Academic Press.

Masson, M. E., 2011: A tutorial on a practical bayesian alternative to null-hypothesis significance testing. *Behavior research methods*, **43 (3)**, 679–690.

Nicholls, N., 2001: Commentary and analysis: The insignificance of significance testing. *Bulletin of the American Meteorological Society*, **82 (5)**, 981–986.

Noer, G., 2018: Article on polar lows, accesed: 2018-08-01. Store Norske Leksikon, `https://snl.no/polart_lavtrykk`.

Økland, H., 1998: Modification of frontal circulations by surface heat flux. *Tellus A: Dynamic Meteorology and Oceanography*, **50 (2)**, 211–218.

Papritz, L., S. Pfahl, H. Sodemann, and H. Wernli, 2015: A climatology of cold air outbreaks and their impact on air–sea heat fluxes in the high-latitude south pacific. *Journal of Climate*, **28 (1)**, 342–364.

Papritz, L. and T. Spengler, 2017: A lagrangian climatology of wintertime cold air outbreaks in the irminger and nordic seas and their role in shaping air–sea heat fluxes. *Journal of Climate*, **30 (8)**, 2717–2737.

Rasmussen, E. A. and J. Turner, 2003: *Polar Lows : Mesoscale Weather Systems in the Polar Regions*. Cambridge University Press, Cambridge.

Renfrew, I. A. and J. C. King, 2000: A simple model of the convective internal boundary layer and its application to surface heat flux estimates within polynyas. *Boundary-layer meteorology*, **94 (3)**, 335–356.

Renfrew, I. A. and G. Moore, 1999: An extreme cold-air outbreak over the labrador sea: Roll vortices and air–sea interaction. *Monthly Weather Review*, **127 (10)**, 2379–2394.

Shumway, R. and D. Stoffer, 2017: *Time Series Analysis and Its Applications: With R Examples*. Springer Texts in Statistics, Springer International Publishing, URL `https://books.google.no/books?id=PTkoMQAACAAJ`.

Smith, E. T. and S. C. Sheridan, 2018: The characteristics of extreme cold events and cold air outbreaks in the eastern united states. *International Journal of Climatology*, **38**, e807–e820.

Stull, R. B., 2012: *An introduction to boundary layer meteorology*, Vol. 13. Springer Science & Business Media.

Taylor, K. E., R. J. Stouffer, and G. A. Meehl, 2012: An overview of cmip5 and the experiment design. *Bulletin of the American Meteorological Society*, **93 (4)**, 485–498.

Vallis, G. K., 2017: *Atmospheric and oceanic fluid dynamics*. Cambridge University Press.

Ventura, V., C. J. Paciorek, and J. S. Risbey, 2004: Controlling the proportion of falsely rejected hypotheses when conducting multiple tests with climatological data. *Journal of Climate*, **17 (22)**, 4343–4356.

Wacker, U., K. V. J. Potty, C. Lüpkes, J. Hartmann, and M. Raschendorfer, 2005: A case study on a polar cold air outbreak over fram strait using a mesoscale weather prediction model. *Boundary-Layer Meteorology*, **117 (2)**, 301–336.

Wallace, J. M. and P. V. Hobbs, 2006: *Atmospheric science: an introductory survey*, Vol. 92. Elsevier.

Walpole, R. E., R. H. Myers, S. L. Myers, and K. Ye, 2014: *Probability and statistics for engineers and scientists*. Pearson London.

Warner, T. T., 2010: *Numerical weather and climate prediction*. Cambridge University Press.

Wilks, D., 2006: On "field significance" and the false discovery rate. *Journal of applied meteorology and climatology*, **45 (9)**, 1181–1189.

Wilks, D. S., 2011: *Statistical methods in the atmospheric sciences*, Vol. 100. Academic press.

Yang, S., S. Gao, and C. Lu, 2014: A generalized frontogenesis function and its application. *Advances in Atmospheric Sciences*, **31 (5)**, 1065–1078.

Zauderer, E., 2011: *Partial differential equations of applied mathematics*, Vol. 71. John Wiley & Sons.